

Re: Authors Reply to Review nhess-2021-280- RC2

Dear reviewer,

We would like to thank you for reviewing our paper, “Ground motions variability in Israel from 3-D simulations of M 6 and M 7 earthquakes” (nhess-2021-280).

Thank you for the time spent and effort. Your remarks and critique certainly improved the manuscript.

Attached below is our pointwise reply to the comments. All the changes and additions appear in the revised version of the manuscript.

All the co-authors approved the revision.

Please address all correspondence to:

Jonatan Glehman

Department of Earth and Environmental Sciences

Ben Gurion University of the Negev

Beer-Sheva 8410501

Israel.

[\(glechman@post.bgu.ac.il\)](mailto:glechman@post.bgu.ac.il)

Nat. Hazards Earth Syst. Sci. Discuss., referee comment RC2
<https://doi.org/10.5194/nhess-2021-280-RC2>, 2022 ©
Author(s) 2022. This work is distributed under the Creative
Commons Attribution 4.0 License.



Comment on nhess-2021-280

Anonymous Referee #2

Referee comment on "Ground motions variability in Israel from 3-D simulations of M 6 and M 7 earthquakes" by Jonatan Glehman and Michael Tsesarsky, Nat. Hazards Earth Syst. Sci. Discuss., <https://doi.org/10.5194/nhess-2021-280-RC2>, 2022

The authors use 3d simulation model to generate M6 and M7 seismic ground motion for Israel, considering local site effects, and source effects (directivity effects and supershear ruptures). Based on the generated data, they develop a local ground motion model (AM) M based solely on M6 and M7 and few rupture scenarios, and compare it with CB14 model.

The key objective of this work is not clear.

Reply: We have tried to clearly state the objective, in the original manuscript (please refer to lines 167 - 172 and 415-416). We have emphasized the objective in the revised manuscript. Please refer to lines: 167-173 and 459-461 in the revised manuscript. Thank you.

The authors conclude that it is important to develop local GMM for Israel considering local sources, path and site effects.

Reply: it is indeed one of our conclusions.

The authors do not explicitly show the simulation model used, nor the parameters or assumptions.

Reply: We provide the essential model input in the original manuscript. Please refer to Figure 4 and Tables 1(density, velocity, quality factors), 2 (grid and source time function) and 3 (simulated scenarios. Also please refer to section 3.1 and lines 264-267 (section 4.1) in the revised manuscript for the assumptions. We believe the data provided sufficiently describes the numerical models and scenarios.

The authors do not validate the results of their simulations.

Reply: Thank you for this comment. Strong motion instrumental record for Israel is not available (see the description in section 2.1), thus we cannot directly validate our model. The work of Shani-Kadmiel et al., (2016) who modelled the Jericho 1927 earthquake (the only M 6 earthquake in the catalogue) used similar numerical platform, similar source model (DSM) and a basic velocity model. The results of this work show good agreement between the reported and the calculated intensities. We consider this work as partial validation of our approach and model. We added this information to lines: 217-219 in the revised manuscript.

The authors claim that the results are model dependent (L414).

Reply: Indeed. We state that to emphasize that the purpose of this study was not a development of an inclusive ground motion model but to study ground motion variability.

The authors do not compare their work with other papers in the region, or hybrid models (eg. please refer to Fayjaloun et al., 2021: Hybrid Simulation of Near-Fault Ground Motion for a Potential Mw 7 Earthquake in Lebanon).

Reply: Thank you for this comment. We would like to point out that the work of Fayjaloun et al., 2021 was published in October 2021, whereas our manuscript was submitted for review on 29.9.21. The comparison of simulated ground motions from different geological settings and different modelling assumptions (1-D to 3-D) may be limited. For example, several works showed that structural and material heterogeneity of the crust in Israel results in regional ground motions variability (Shimony et al., 2021; Volk et al., 2017). These can only be captured by 3-D modelling. We acknowledge the work of Fayjaloun et al., 2021 in the revised manuscript (lines 454 - 458). As there are no other works of 3D simulated M 7 ground motions in Israel, we cannot compare our simulations with other databases. However, we compare our results with global GMPE's as they are based on the ergodic assumption and account for some site effects.

The authors do not clarify their choice of the attenuation functional model (please refer to <http://www.gmpe.org.uk/gmpereport2014.pdf>).

Reply: Thank you for this comment. The functional form of our attenuation model (AM) is based on the CB-14 function model. We also modified the Z_2 and $V_{s,ref}$ terms accordingly. Following your suggestion, we added this information to the revised manuscript, lines 280-282.

The authors validate the estimation of AM and of CB14 to the simulated GM: they find out that AM works better (which is obviously coming from the regression analysis using the same database) and conclude that CB14 ('imported GMM') deviates from the simulated GM.

Reply: Thank you for this comment. You are right. The comparison with AM may seem redundant, but it is essential to show that it still deviates from the simulations even though it is based on it, and future refinements are needed. The CB-14 is indeed performing differently than our simulations. We do not compare the CB-14, and the AM as the AM was constructed not as a ground motion model but to examine the variability of the ground motions.

The authors do not justify the choice of CB14 model to compare their work in this region, considering that CB14 do not take directivity into account.

Reply: We choose CB-14 as it is a development of the CB-08 used in the Israel building code (413) and is planned to supersede it. Also, CB-14 is one of the NGA-West 2 based empirical ground-motion models widely used globally. To our best knowledge, none of the empirical models account for directivity. Thus, it is one of the reasons to develop a region-specific ground motion model accounting for such effects. We added this information to lines: 345-346 in the revised manuscript.

Please show: Gilboa and Carmel faults in figure 1.

Reply: Thank you for the suggestion. Gilboa and Carmel faults are parts of the Carmel Fault System (CFZ, please refer to lines: 95-96 in the revised manuscript) presented in Figure 1.

L97: the DSF magnitude potential of up to Mw7.5 (Hamiel et al., 2009).

Reply: Correct. We added the relevant value in line 97 in the revised manuscript. Thank you.

L 99- 101: the information are not fully coherent with Nof. et al 2021 (TRUAA—Earthquake Early Warning System for Israel: Implementation and Current Status).

Reply: Thank you for pointing it out. We modified our manuscript accordingly. The updated information can be found in lines: 100-101 and 105 in the revised manuscript.

Better use the official name of the TRUAA project (instead of Tru'a)

Reply: Thank you for pointing it out. Modified, lines: 104 and 122.

L 129: I would recommend the author to dedicate a few lines to better describe the spatial heterogeneity of the Earth structure.

Reply: Thank you for this comment. please refer to section 2.2 "Spatial heterogeneity of Israel", in the revised manuscript.

L135: please add reference

Reply: Added to line 142 of the revised manuscript. Thank you.

L189: I would recommend a few lines to describe the software, the (dynamic ?) simulations, how does it consider the source, propagation and site effects, the assumptions made, the choice of the nucleation point

Reply: Thank you for this comment. The necessary information was provided in section 3.1 "Numerical model" and tables: 1,2 and 3.

L 234-236: the authors choose rupture speed to be equal to $0.9V_s$ and $1V_s$ for subshear and supershear scenarios respectively. please justify this, knowing that the rupture speed should be lesser than $0.85V_s$ or larger than $1.2V_s$.

Reply: Rupture speed values usually vary between $0.6-0.9 V_s$. (see for example Heaton, 1990). We chose $0.9V_s$, as this value is widely used in the literature, see for example (not an inclusive list) works of: Kaneko and Shearer (2014); Bizzarri and Spudich, (2008); Lin et al., (2020); Liu et al., (2014); Weng and Ampuero (2020). As per the supershear speed, the rupture nucleates within the hard rock with a subshear speed of 1800 m/s. It evolves into supershear rupture when it ruptures the sediments with shear wave velocity of <900 m/s (greater than the Eshelby speed $1.41V_s$, as predicted for supershear ruptures). Please refer to lines: 243-245 in the revised manuscript.

L252: why 129 GM simulations seem sufficient?

Reply: We have attained 129 records for each simulation (five for each magnitude). Total of 633 and 645 ground motion records for M 7 and M 6 scenarios. First, we deployed a uniform grid with 10 km spacing (total of 124 synthetic stations). Following we added five more stations in areas of interest (such as Zevulun Valley, Kiryat Shemona, among others). This deployment provides sufficient spatial coverage to account for ground motion variations. The ground motion model will be further constrained with more ground motion records. We added this information to lines 188-190 in the revised manuscript.

L 352: Can the authors explain why the duration of the simulated GM is not function of the distance?

Reply: Thank you for this comment. We added this information to lines 378-380 and 449-450 in the revised manuscript.

L 399: please explicitly show how you notice this conclusion from the AM. do you notice the same conclusion with your simulated ground motion ?

Reply: Thank you for this comment. We modified Figure 6 to represent our results better, and to properly differentiate between residuals associated with source effects from those associated with path and site effects. The AM adopts a typical form of ground motion model. Figures 6c,d show that the within-events residuals (δw) are path-dependent for the directivity and supershear scenarios. Whereas Figures 6e,f clearly show that the between events residuals (δB) related to source effects are not zero for the supershear scenario (however, they are equal to zero for the directivity scenario). This means that additional path terms should be incorporated in the AM for the directivity and supershear ruptures, and additional source terms for supershear ruptures.

L 415-416: you can not study the variability of the ground motion with a model that is not validated.

Reply: Thank you for this comment. As we explained above the main challenge in Israel is the low seismicity rate which results in a $M > 6$ gap in the instrumental catalogue. Using low magnitude events would not provide the necessary validation as the details of finite fault kinematics of $M > 6$ earthquakes are not covered by point source models. Furthermore, the spatial coverage of the ISN (at least till 2020) is sparse and doesn't cover areas of interest. This being the case, validation *sensu-stricto*, is not within reach. We do report the Shani-Kadmiel (2016) work as a benchmark. We further develop the velocity model, both near the faults and in the regions of interest to provide a more refined model. This model clearly shows ground motions variability, compared to reference models. We report the results with the necessary caution and do not claim that these results should (or could be used) as is. We added this information to lines: 217-219 in the revised manuscript.

L434: this statement is not a result of your work and thus should not be described in the summary section.

Reply: we accepted the suggestion and rewrote this paragraph.

figure 1:

- better resolution ?

Reply: modified. Thank you.

- b. please define PA in the caption.

Reply: Added. Line 120 in the revised manuscript. Thank you.

- b. I would recommend the authors to change the description: 'the Israel seismic network in Israel: yellow.. and brown .. . the green circles show the population ..'

Reply: Thank you for the suggestion. However, we believe that the current formulation contributes better to the caption's flow.

figure 2:

plot Y in logarithmic scale ?

Reply: Thank you for the suggestion. However, there is no need for a logarithmic scale as Y-axis values are of one order of magnitude.

figure 3:

- show the location of the vs profile on plot (a)

Reply: Locations added. Thank you.

- what is the reference of this plot what do the yellow and purple colors represent ? figure 5, 6, 10:

Reply: Thank you for this comment. The color description was added to lines 175-176 in the revised manuscript. For references to the plot, please refer to section 2.2, "Spatial heterogeneity of Israel."

- use the same color legend for M6 and M7 figure 10: remove 'comparison' from the caption description.

Reply: Color legend modified. We rewrote the caption's description. Please refer to line 392 in the revised manuscript. Thank you.

Ground motions variability in Israel from 3-D simulations of M 6 and M 7 earthquakes

Jonatan Glehman¹ and Michael Tsesarsky^{1,2}

¹Department of Earth and Environmental Sciences, Ben Gurion University of the Negev, 8410501, Israel

²Department of Civil and Environmental Engineering, Ben Gurion University of the Negev, 8410501, Israel

Correspondence to: Jonatan Glehman (glehman@post.bgu.ac.il)

Abstract. In Israel, due to low seismicity rates and sparse seismic network, the temporal and spatial coverage of ground motion data is insufficient to estimate the variability of moderate-strong ($M > 6$) ground motions required to construct a local ground motion model (GMM). To fill this data gap and to study the ground motions variability of $M > 6$ events, we performed a series of 3-D numerical simulations of M 6 and M 7 earthquakes. Based on the results of the simulations, we developed a parametric attenuation model (AM) and studied the residuals between simulated and AM PGVs and the single station variability. We also compared the simulated ground motions with a global GMM in terms of peak ground velocity (PGV) and significant duration (D_s 595). Our results suggested that the AM was unable to fully capture the simulated ground motions variability, mainly due to the incorporation of super-shear rupture and effects of local sedimentary structures. We also showed that an imported GMM considerably deviates from simulated ground motions. This work sets the basis for future development of a comprehensive GMM for Israel, accounting for local sources, path, and site effects.

1 Introduction

The recent report by the Centre for Research on the Epidemiology of Disasters (CRED) and the UN Office for Disaster Risk Reduction (UNDRR) – Human Cost of Disasters, 2000 - 2019 – clearly shows that earthquakes are the deadliest natural disasters. Accounting for only 3 % of the total number of people affected by natural disasters, they count for 58 % of deaths (more than 700,000) of all disaster types and 21 % of recorded economic losses (Mizutori and D’ebarati, 2020). Over the past 40 years, the global population exposed to a moderate to severe intensity earthquake has increased by 93 % (to 2.7 billion people) (Pesaresi et al., 2017). This value is expected to grow with population growth and increasing urbanization.

Seismic hazard is the intrinsic natural occurrence of earthquakes and the resulting ground motion and other effects (Wang, 2005). Ground motion models (GMM’s) are critical components in the mitigation of seismic hazard. Empirically based GMMs, also known as Ground Motion Prediction Equations (GMPE’s), are parametric models that estimate the median and the variability of the expected ground motions at a site. The main explanatory variables of such models are typically earthquake magnitude, distance, and site conditions. New generation GMMs also address faulting style, depth to rock, and others.

Many regions worldwide, either due to low seismicity rates and/or sparse coverage of the seismic network, do not provide sufficient temporal and spatial data to estimate the variability of ground motions required to construct a local GMM or validate an imported GMM to local conditions. This situation is specifically acute in the range of strong earthquakes at relatively short distances that pose the most significant hazard to human life and infrastructure.

37 The use of imported GMM's under the ergodic assumption attributes the ground motion variability to the
38 randomness of the process (i.e., aleatory variability) rather than to local systematic source-path and site effects
39 (i.e., epistemic uncertainty) (Anderson and Brune, 1999). Abrahamson et al., (2019) showed that the increased
40 number of strong-motion records over the past decade exhibit significant differences in scaling of the ground
41 motions even within relatively small regions and that most of the variability typically treated as aleatory is actually
42 due to systematic source, path, and site effects. Kuehn et al., (2019) showed the importance of variations in quality
43 factor (Q) over small spatial scales (30 km) in California. Specifically showing that accounting for path effects
44 leads to a smaller value of the aleatory variability and results in different median predictions, depending on source
45 and site location. To achieve this improvement, Kuehn et al., (2019) divided California into a grid with a cell size
46 of 30 km by 30 km and used 12,039 records from 274 events recorded at 1504 stations. This approach can be
47 employed only in data-rich regions, such as California. Lan et al., (2019) showed that for South Western China,
48 imported GMM's result in significant discrepancies compared with regional instrumental data (including the
49 Wenchuan Mw 7.9 event). In addition, despite the recorded ground motion data expanding, it remains sparse for
50 large, complex ruptures with recurrence intervals generally exceeding the observation length of instrumental
51 records.

52 The challenges met while predicting ground motion in data-poor regions turn numerical modeling into an
53 essential complementary method for seismic hazard analysis (Chaljub et al., 2010). Numerical modeling alleviates
54 the need for the ergodic assumption, as it can augment the seismic data with strong motion records and account
55 for ground motions variability by systematically separating source, path, and site effects. For example, Graves et
56 al., (2011) showed that the combination of rupture directivity and basin response effects could lead to an increased
57 hazard in particular sites, relative to that calculated by GMM. Pitarka et al., (2021) found that the combination of
58 rupture propagation effects with the amplification due to local topography can result in large ground motions
59 amplifications with complex spatial variability.

60 However, the shift from ergodic models to nonergodic models, which account for local source-site and
61 path effects such as numerical models, leads to large epistemic uncertainty in the median ground motion, resulting
62 in increased epistemic uncertainty of the hazard (Walling and Abrahamson, 2012). Such uncertainty is derived
63 from both modeling and parametric uncertainties, as the model, is not well constrained. Model uncertainty can be
64 reduced by using more accurate 3D crustal models and source models.

65 Subsurface models with different levels of accuracy and completeness are available around the world. With
66 the increasing use of terrestrial and space geodesy, the control of seismic sources is also improving with time.
67 Combining the two enables the construction of numerical models for regional assessment of ground motions
68 (Pitarka et al., 2021; Douglas and Aochi, 2008; Graves and Pitarka, 2015). A hybrid GMM, based on empirical
69 and synthetic ground motion databases, is expected to reduce the epistemic uncertainty of the median ground
70 motion and will lead to a lower aleatory variability than GMM's based on data with limited magnitude and distance
71 bands.

72 In Israel, low seismicity rates (centennial and millennial return periods) and a limited instrumental catalog,
73 spanning only four decades and contain mainly $M < 6$ events, impede the development of local empirical GMM.
74 The practical outcome of this shortcoming is the use of imported GMM's, such as the Campbell & Bozorgnia,
75 (2008; hereafter, CB08) used in the Israel Seismic Design Code IS 413 (Israel Standards Institution, 2013).

76 Contrary to the instrumental catalog, the Israel pre-instrumental catalog spans over three millennia (Agnon, 2014),
77 including numerous $M > 6$ events, with up to 14 $M > 7$ events.

78 This paper presents numerical modeling of ground motions in Israel, intended to narrow the strong ground
79 motion data gap and study ground motions variability from moderate ($M 6$) and strong ($M 7$) earthquakes. We
80 begin with a brief introduction to the seismo-tectonic setting of the region. Then, we proceed to the methodology
81 section to describe the process of generating a synthetic ground motion database and the subsequent construction
82 of a parametric ground motion model. The results section presents the simulated ground motions and the respective
83 attenuation model. Then, it compares it with the global GMM's of Campbell & Bozorgnia, (2014; hereafter,
84 CB14) and Afshari & Stewart, (2016) performance with respect to the synthetic database. Finally, we discuss our
85 findings and provide insights regarding the seismic hazard from moderate to strong earthquakes and the
86 importance of developing a comprehensive regional GMM to mitigate the seismic hazard in Israel.

87 **2 The seismo-tectonic setting of Israel**

88 **2.1 Seismicity and seismic hazard in Israel**

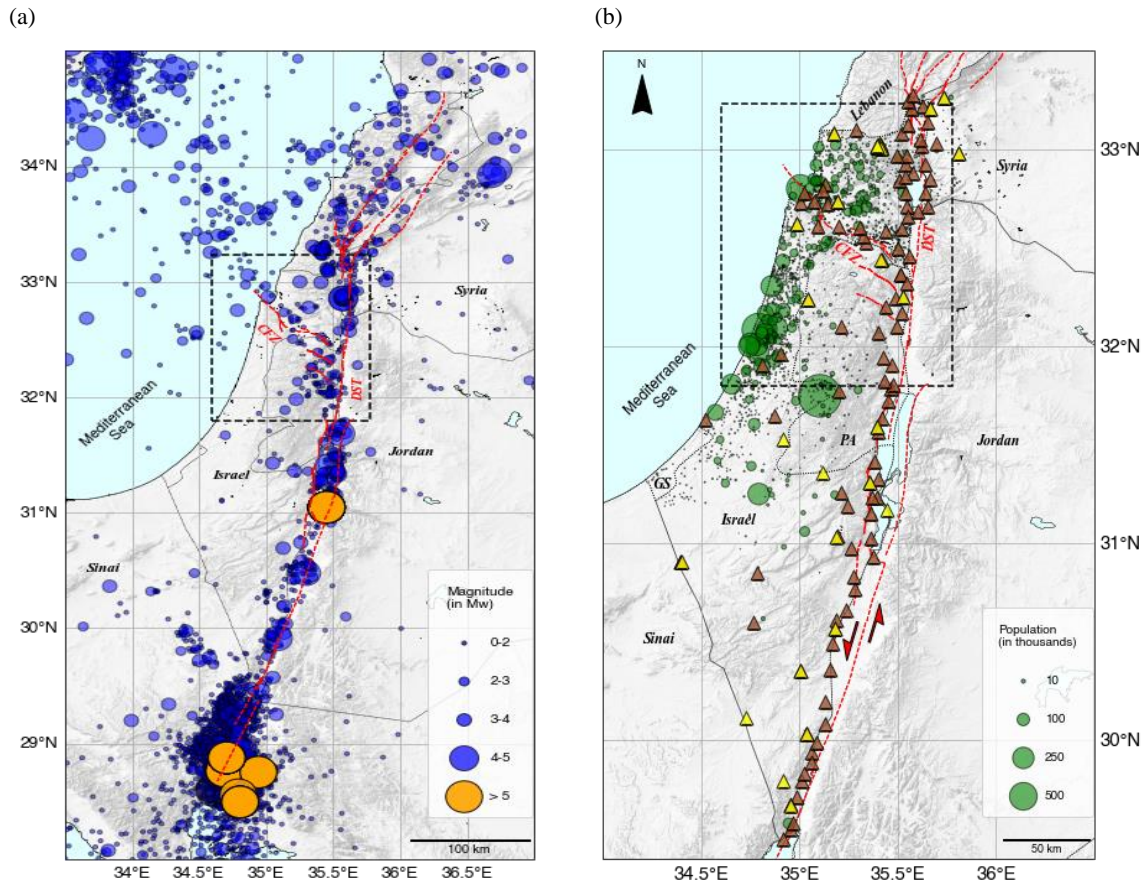
89 The Dead Sea Transform (DST) fault system is an active tectonic boundary separating the African and Arabian
90 plates. Extending from the Gulf of Aqaba to southern Turkey, a total length of approx. 1100 km, it dominates the
91 seismicity of Israel, Palestinian Authority, Lebanon, and Syria (Fig. 1a,b). The DST is a left-lateral strike-slip
92 fault with a total offset of 105 km (Garfunkel, 2014). The average long-term slip rate is 4 to 5 mm year⁻¹ (Bartov
93 et al., 1980). Geodetic slip rates along the Israeli part of the DST range from 3 to 5 mm year⁻¹ (Hamiel et al., 2016;
94 Sadeh et al., 2012).

95 Splaying north-west from the DST is the Gilboa Fault, and farther north-west towards the Mediterranean,
96 the Carmel Fault. Both comprise an active zone generalized as the Carmel Fault Zone (CFZ). The DST segments
97 are capable of producing $M 6$ and $M 7-7.5$ events (Shamir et al., 2001; Hamiel et al., 2009), and the CFZ is capable
98 of producing up to $M 6.5$ earthquakes (Grünthal et al., 2009).

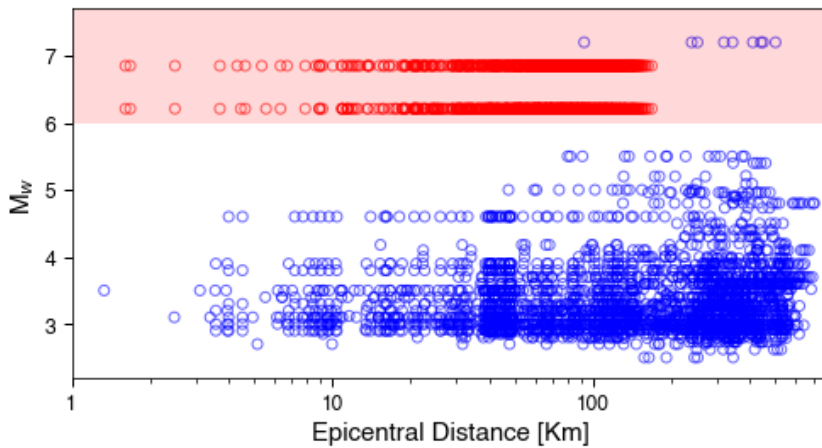
99 The Israel Seismic Network (ISN), established in 1983 and upgraded over the years, consists of a mixture
100 of different instrumental and operational stations, including short-period stations (14 in total), broadband stations
101 (24 in total), and a large broadband array (part of the Comprehensive Nuclear Test Ban Treaty). The deployment
102 of the ISN does not cover areas of increased seismic hazard, e.g., densely populated zones and soil sites, or areas
103 designated by the Israel Seismic Code (IS413) as suspected in extreme ground motion amplification, such as the
104 Zevulun Valley (Fig. 1b). Currently, the seismic network is upgraded within the TRUAA project (an early warning
105 system), with up to 69 strong-motion accelerometers and 12 broadband seismometers added to ISN (Kurzon et
106 al., 2020). However, most of the instrumentation are placed along the DST and Carmel fault to provide early
107 warning, and not in densely populated or industrialized areas where the seismic risk is tangible. Based on
108 demographic projections (the Taub Center for Social Policy Study in Israel; For URL see data and resources) the
109 population of Israel is expected to grow from 9.05 million in 2021 to 12.8 million in 2040 and combined with the
110 increasing demand for housing and infrastructures, the seismic risk is expected to grow.

111 The Israel seismic catalog covers 36 years of measurements (1985–2021) and includes more than 23,300
112 events (Wetzler & Kurzon,2016), but only 15 of them are of $M > 5$ (Fig. 1a and Fig. 2). Moving back in time,
113 Israel's pre-instrumental catalog spans over 3000 years (Agnon, 2014; Zohar, 2019) with many catastrophic

114 events, such as the 749 ($M > 7$), 1202, ($M > 7.5$), 1759 ($M > 7$), and the 1837 ($M > 7$) earthquakes, among others.
 115 In total, fourteen $M > 7$ events were cataloged by Ambraseys (2006) in the past two millennia. Recent geodetic
 116 studies (Hamiel et al., 2016; Sadeh et al., 2012) identified a slip deficit on specific segments of the DST, such as
 117 the Jordan Gorge Fault (JGF) and the Jordan Valley Fault (JVF), equivalent to an $M > 7$ earthquake.



118 **Figure 1.** (a) Israel Seismic catalog (M_w) for the period 1985-2021 orange circles are events with $M_w > 5$ (expansion of
 119 Wetzler & Kurzon (2016) catalog). Red lines are active tectonic borders and faults, DST is Dead Sea Transform, CFZ is
 120 Carmel Fault Zone. (b) Demographics of Israel and the Palestinian Authority (PA) and the deployment of the Israel Seismic
 121 Network. Yellow triangles are the old (up to October 2017) Israel Seismic network stations, brown triangles are the current
 122 (TRUAA) seismic network stations. (after Kurzon et al., (2020)). GS is Gaza Strip. The black rectangles define the
 123 computational domain presented in Fig. 3a.



124
 125 **Figure 2.** Israel's ground motion database (blue circles) for the period 1983-2021 as a function of epicentral distance (Yagoda-
 126 Biran et al., 2021). The shaded rectangle spans the $M_w > 6$ region of moderate-strong ground motion records. The red circles
 127 are the simulated ground motions from this work.

128 2.2 Spatial heterogeneity of Israel

129 The geological structure of Israel exhibits strong spatial heterogeneity over short scales (Fig. 3a,b). Deep pull-
 130 apart basins (up to 10 km) filled with soft sediments ($V_s \sim 600\text{-}800 \text{ m sec}^{-1}$) accompany the active DST system,
 131 from south to north: The Dead Sea Basin, Beit Shean Valley (BSV), the Sea of Galilee (SG) and the Hula Valley
 132 (Rosenthal et al., 2019). Along the CFZ, the Zevulun, Harod, and Jezreel Valleys are formed. The vulnerability
 133 of Zevulun Valley is particularly crucial because of its dense population and the high concentration of strategic
 134 industrial infrastructure (Shani-Kadmiel et al., 2020).

135 The Israeli coastal plain, one of the most densely populated regions of the country (on average, 9000 people
 136 per km^2), is underlain by a westward thickening sedimentary wedge (SW). In the Judea foothills area, east of the
 137 SW, a strong reflector exists between the sandstones and clays (Pleistocene Kurkar Gr, $V_s \sim 300 \text{ m sec}^{-1}$) and the
 138 hard carbonate rocks (the Cretaceous Judea Gr., $V_s \sim 2000 \text{ m sec}^{-1}$). In the coastal plain, the Kurkar Gr. overlays
 139 the soft carbonates (Avedat Gr, $V_s \sim 900 \text{ m sec}^{-1}$) and clastic sediments (the Bet Guvrin Fm., $V_s \sim 800 \text{ m sec}^{-1}$)
 140 (refer to Fig. 3b). The depth of the Kurkar Gr. base reflector is typically several tens of meters. Further to the west,
 141 a prominent reflector is a contact between the clays (Pliocene Yafo Fm., $V_s \sim 600 \text{ m sec}^{-1}$) and top of Judea Group
 142 (Gvirtzman et al. 2008). These two reflectors, when shallower than 250 m, were used for the latest update of the
 143 Israel Building Code IS 413 (Israel Standards Institution, 2013) to delineate areas of high potential of ground
 144 motion amplification (Gvitzman and Zaslavsky, 2009). This situation further complicates the process of
 145 developing an empirical GMM for Israel.

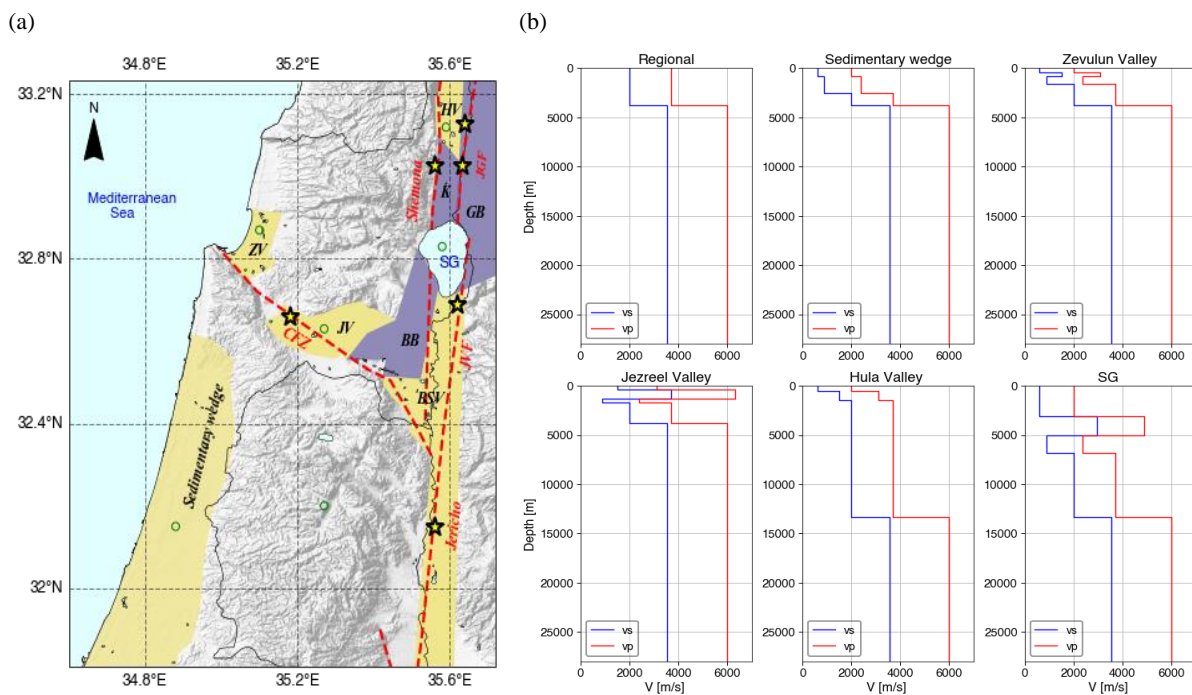
146 2.3 Source effects

147 The impact of inter-basin sources along the DST on regional ground motions was examined by Shimony et al.,
 148 (2021). This work clearly showed that regional ground motions are determined by source-path coupling effects in
 149 the strike-slip basins before waves propagate into the surrounding areas. Ground motions are determined by the
 150 location of the rupture nucleation, the near-rupture lithology, and the local structures. Shimony et al., focused on
 151 symmetric sub-shear ruptures and did not model rupture directivity or super-shear rupture velocities, both known
 152 to amplify regional ground motions.

153 Under specific conditions, super-shear ruptures and directivity occur on bi-material faults (Shi & Ben-Zion
 154 2006). Specifically, for subsonic propagation, symmetrically initiated bilateral rupture evolves after some
 155 propagation distance to a unilateral rupture in the positive direction, which is the direction of slip on the compliant
 156 side of the fault containing the softer layer. The magnitude of this effect increases with propagation velocity and
 157 the degree of material contrast across the fault. At super-shear propagation speeds, along a bi-material fault, the
 158 propagation direction is reversed.

159 The DST is a mature left-lateral fault with a 105 km offset, resulting in strong material contrast between
 160 the hard layers on the Jordan side (east) and the soft layers on the Israeli side (west). Thus, the rupture can
 161 potentially propagate unilaterally southwards, discharging most of the seismic energy into Israel or northward in
 162 super-shear mode. The Jordan Gorge Fault and the Jordan Valley Fault (both active faults of the DST) specifically
 163 can produce an earthquake with rupture propagating in super-shear velocity since they border deep sedimentary
 164 basins, characterized by large shear wave velocities contrast along the rupture propagation path. Thus, to quantify
 165 the seismic hazard ensuing from bi-material faults, it is necessary to study the two propagation directions; both
 166 sub-shear and super-shear velocities.

167 The primary purpose of this work is to study the different source, path, and site effects of simulated, M 6
 168 and M 7 earthquakes and their contribution to ground motion variability in Israel. To this end, we have improved
 169 the 3-D regional velocity model of Shimony et al., (2021) and numerically modeled M 6 and M 7 earthquakes with
 170 different source and path properties. Following, we developed a parametric model of median ground motions and
 171 their variability, in terms of Peak Ground Velocity (PGV). The model quantifies the spatial distribution of the
 172 ground motions in central and northern Israel, accounting for source, path, and site effects, including rupture
 173 velocity and directivity.



174 **Figure 3.** (a) The DST fault system and the Carmel Fault Zone (CFZ) and accompanying structures. Sedimentary structures
 175 (yellow): BSV-Beit Shean Valley, ZV-Zevulun Valley, JV-Jezreel Valley, HV-Hula Valley, SG-Sea of Galilee, and the
 176 Sedimentary wedge; and hard rock structures (purple): K-Korazim structural saddle, BB-Belvoir Basalts, GB-Golan Basalts.

177 The yellow stars indicate the epicenter of the seismic sources simulated in our work: Jordan Gorge Fault (JGF), with bilateral
178 and unilateral slip realization, Jordan Valley Fault (JVF), Jericho Fault, Shemona Fault (only for M 7), and CFZ (only for M
179 6). (b) Representative depth velocity profiles of the computational domain (green circles).

180 **3 Methodology and workflow**

181 Developing a regional GMM for Israel requires a database of ground motion records, including $M > 6$ events at
182 short, <100 km, distances. To supplement the existing ground motions database, we added a suite of synthetic
183 ground motions from physics-based 3D numerical models of different M 6 and M 7 earthquakes (Fig. 2).

184 Our work comprised two main stages; first, we modified and expanded the regional velocity model of
185 Shimony et al., (2021), to represent a more realistic geological setting and contain the Golan Basalts, the central
186 part of Israel, and the sedimentary wedge. Then, we simulated five different earthquake scenarios for each
187 magnitude, with nucleation at different locations along the DST and CFZ. For each scenario, we recorded synthetic
188 ground motions at 129 stations (see supplementary material, Fig. S1), with 124 stations deployed in a uniform
189 grid with 10 km spacing and five more stations in areas of interest (such as Zevulun Valley, Kiryat Shemona,
190 among others). Next, we performed statistical analysis of the synthetic database, using multivariable regression,
191 by minimizing residuals between data and model estimations. We then formulated a parametric model of the
192 ground motions and examined its consistency with the simulated database, in terms of the median ground motions
193 and their variability for each of the simulated scenarios.

194 **3.1 Numerical model**

195 Ground motions in this research were modeled using the SW4v2 software (Petersson and Sjogreen, 2014, 2017a,
196 b), developed for large-scale simulations of seismic wave propagation on parallel computers.

197 The velocity model covers the northern and central part of Israel (fig. 4a) and includes the main DST trough
198 and the following basins/structures, from south to north: Beit Shean Valley (BSV), Belvoir Basalts (BB), Sea of
199 Galilee (SG), Korazim structural saddle (K), Golan Basalts (GB) and Hula Valley (HV). Along the CFZ, we model
200 the major sedimentary basins of Jezreel Valley (JV) and Zevulun Valley (ZV). The coastal plain is underlain by
201 the westward thickening Sedimentary wedge (SW). Geographically, the model extends from the city of Ashdod
202 in the south (31.8° N, 34.6° E) to Hula Valley in the north (33.23° N, 35.72° E) and from the Mediterranean Sea
203 in the west to the Golan Basalts in the east. Figures 4b,c,d illustrate the north-south and east-west cross-sections
204 of the velocity profiles. The numerical domain spans 159 km in the north-south direction and 124 km in the east-
205 west direction. It covers almost 80 % of the Israeli population and a significant part of the population of the
206 Palestinian Authority.

207 Subsurface geometry and the characteristics of the DST trough were obtained from Rosenthal et al., (2019)
208 with modifications for the Hula Valley, obtained from the density log of the Notera 3 (Rybakov et al., 2003). The
209 sedimentary wedge structure retrieved from Gvirtzman et al. (2008) and the Zevulun Valley structure was set
210 using data from Gvirtzman et al. (2011). The basement depth along the model is based on Ben-Avraham et al.,
211 (2002). Five physical quantities describe the viscoelastic material model used in this research: shear wave velocity
212 (V_s), pressure wave velocity (V_p), density (ρ), and seismic quality factors (Q_s , Q_p) for each point in the
213 computational space. The missing parameters were assessed indirectly by using the correlation presented by
214 Brocher (2008). The main units with their respective velocity, density and quality factors are shown in Table 1.

215 Seismic sources were modeled using the distributed slip model (DSM) developed by Shani-Kadmiel et al.,
216 (2016). DSM is a kinematic model which describes the rupture patch as an elliptic surface with maximum slip at
217 the nucleation point, decaying toward the edges as a pseudo-Gaussian function (Fig. S2). Shani-Kadmiel et al.,
218 (2016) present validation of the DSM using macroseismic reports of the 1927 Jericho earthquake, showing good
219 agreement between the reported and simulated ground motions. Rupture patch size and displacements were scaled
220 following the relations presented in Wells & Coppersmith (1994). All sources were modeled as left-lateral, vertical
221 strike slips (a dip of 90° and rake of 0°), with a strike of 3° for sources on the DST and a strike of 325° for the
222 CFZ. The moment-rate time function of each point on the rupture patch was set to a GaussianInt pulse (Petersson
223 and Sjogreen, 2017b) with a central frequency of $f_0=0.4$ Hz and a maximum frequency of $f_{\max}=1$ Hz.

224 The depth of the model was set to 28 km corresponding to the maximum seismogenic depth in this region
225 (Wetzler and Kurzon, 2016). We assigned a minimum shear wave velocity of 608 m s^{-1} for the uppermost
226 sedimentary layer due to the computational limitations of our system. Grid spacing was set to 76 m in accordance
227 with the minimum shear wave velocity and the maximum frequency of the source. We set the simulation time to
228 120 seconds to allow the slowest waves to propagate across the entire computational domain. The main parameters
229 of the numerical setting are summarized in Table 2.

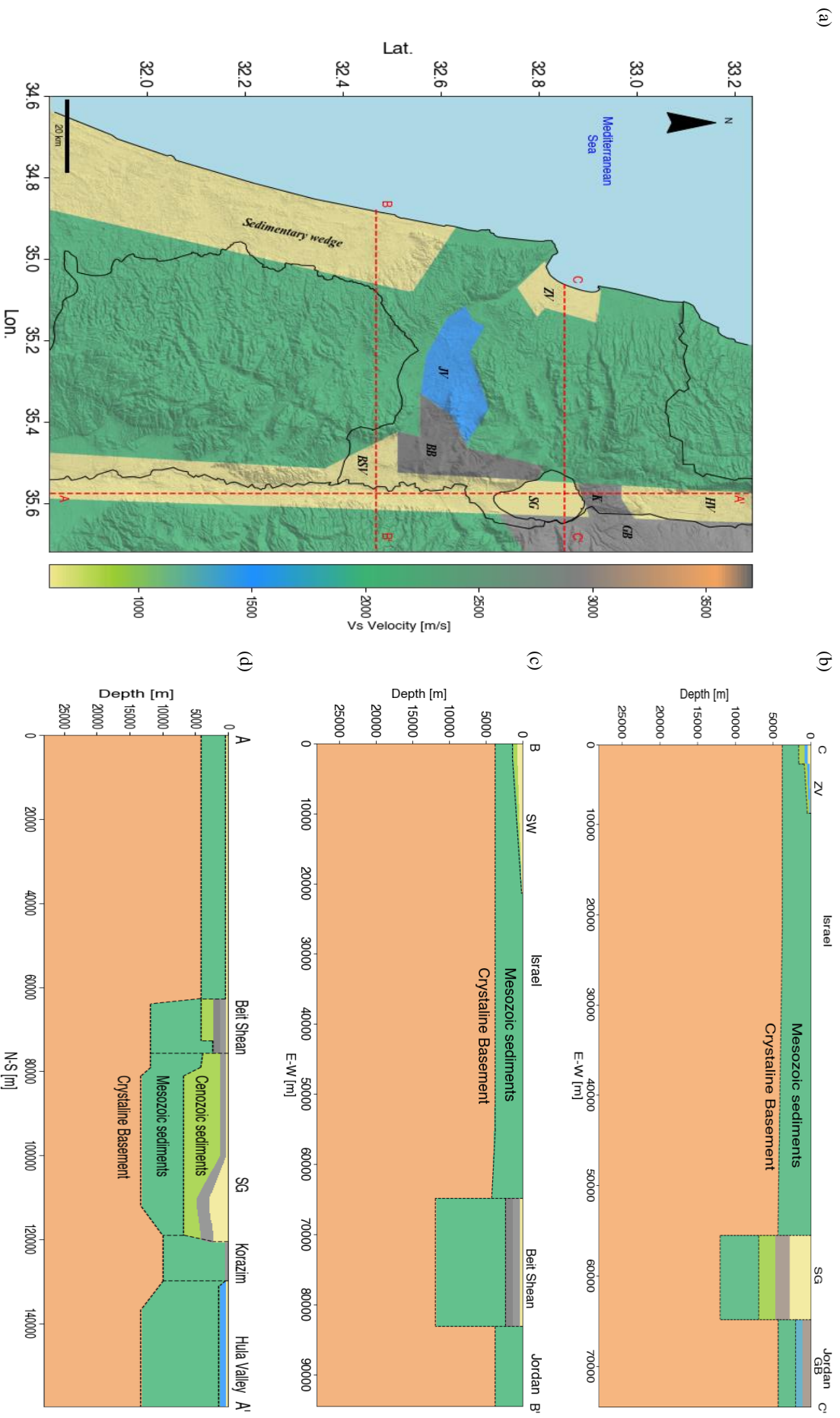


Figure 4. (a) The numerical model of the computational domain accompanied with subsurface cross-sections, marked with red dashed lines: (b) east-west cross section through the Sedimentary wedge, BB' and (d) north-south cross-section through the DST trough, AA'. CC' (c) east-west cross-section through the Sedimentary wedge, BB' and (d) north-south cross-section through the DST trough, AA'.

231 **Table 1.** Material properties of main stratigraphic units used in this work

Model part	Rock Formation	Vs [m s ⁻¹]	Vp [m s ⁻¹]	Qs	Qp	ρ [Kg m ⁻³]
Regional	Crystalline basement	3550	6000	403	806	2720
	Cenozoic and Mesozoic sediments (Judea/ Talme Yafe, Mount Scopus Avedat, and Lower Saqiye)	2000	3700	160	320	2350
Local variations:						
DST	Cenozoic sediments (Umm Sabune, Bira and Gesher)	887	2380	62	124	2054
	Miocene volcanics (lower basalt)	3698	6330	439.5	879	2790
	Pliocene volcanics (upper basalt)	2947	4900	282	564	2520
	Notera/Lisan	608	2000	39.87	79.74	1900
Hula	Cenozoic sediments	1500	3100	111.5	223	2245
	Notera/Lisan	608	2000	39.87	79.74	1900
JV	Cenozoic sediments (Umm Sabune, Bira, and Gesher)	887	2380	62	124	2054
	Miocene volcanics (lower basalt)	3698	6330	439.5	879	2790
	Cenozoic sediments	1500	3100	111.5	223	2245
ZV	Cenozoic and Senonian sediments (Mount Scopus Avedat and Beit Guvrin)	887	2380	62	124	2054
	Cenozoic sediments (Patish)	1500	3100	111.5	223	2245
	Cenozoic sediments (Kurkar and Yafo)	608	2000	39.87	79.74	1900
SW	Cenozoic sediments (Lower Saqiye)	887	2380	62	124	2054
	Cenozoic sediments (Kurkar and Upper Saqiye)	608	2000	39.87	79.74	1900

232 **Table 2.** Main parameters of the numerical model

Parameters	Value
Model Dimensions (L×W×D)	159.63 Km × 124.45 Km × 28 Km
Spatial spacing (dh)	76 m
Grid size (points)	1.27×10^9
Time step spacing	0.0125 s
Simulated time	120 s
Source Dimensions (L×D)	M 6: 32 Km × 15 Km M 7: 38 Km × 22 Km
Source maximum and average slip	M 6: 0.5 and 0.2 m M 7: 3 and 1.57 m
Seismic moment (M_0)	M 6: 2.57×10^{18} N·m (Mw 6.21) M 7: 2.37×10^{19} N·m (Mw 6.85)
Source fundamental (f_0) and maximal frequencies (f_{max})	0.4 and 1 Hz

233 **3.2 Earthquake scenarios and database**

234 To examine the variability of ground motions from moderate M 6 and strong M 7 earthquakes, we concentrated
 235 on earthquake events nucleating on active segments of the DST system, with known slip deficit, and along the

236 CFZ. We modeled a symmetric bilateral rupture on the Jordan Gorge Fault (JGF-B), Jericho Fault (JF) Carmel
 237 Fault Zone (CFZ) and the Shemona Fault (SF), a southward unilateral rupture on the JGF (JGF-U), and a super-
 238 shear rupture on the Jordan Valley Fault (JVF) (Fig. 3).

239 The hypocenter for the DST events was placed in the middle of the seismogenic depth; 11 and 13 Km, for
 240 the M 6 and M 7 respectively, for the M 6 CFZ, the value was set to 12 Km. The rupture patch was designed to
 241 be contained in uniform lithology to prevent super-shear rupture speeds in the shallow parts of our model.
 242 Therefore, rupture speed for each scenario was set to $0.9 V_S$ of the lithology surrounding the nucleation zone. The
 243 only exception was the JVF scenario for both M 6 and M 7, in which we modeled super-shear effects. For this
 244 scenario, the rupture nucleates within the hard rock with a sub-shear speed of 1800 m/s and evolves into supershear
 245 rupture when it ruptures the sediments with shear wave velocity of <900 m/s. The rupture velocity of each scenario
 246 corresponds to the local variations of the sediment's depth. Following the transition of the nucleation zone from
 247 the shallow crystalline basement in the south and west parts of the model to the thick Mesozoic and Cenozoic
 248 sediments in the north and the east, the rupture velocity decreases from 3195 m s^{-1} along the Shemona, Carmel,
 249 and Jericho faults to 1800 m s^{-1} along the JGF and JVF faults. As a reference, we simulated a simple two-layered
 250 reference model (Ref) on the JGF, with mechanical properties similar to the regional setting, following Aldersons
 251 et al., (2003). The scenarios are summarized in Table 3.

252 **Table 3.** Earthquake scenarios

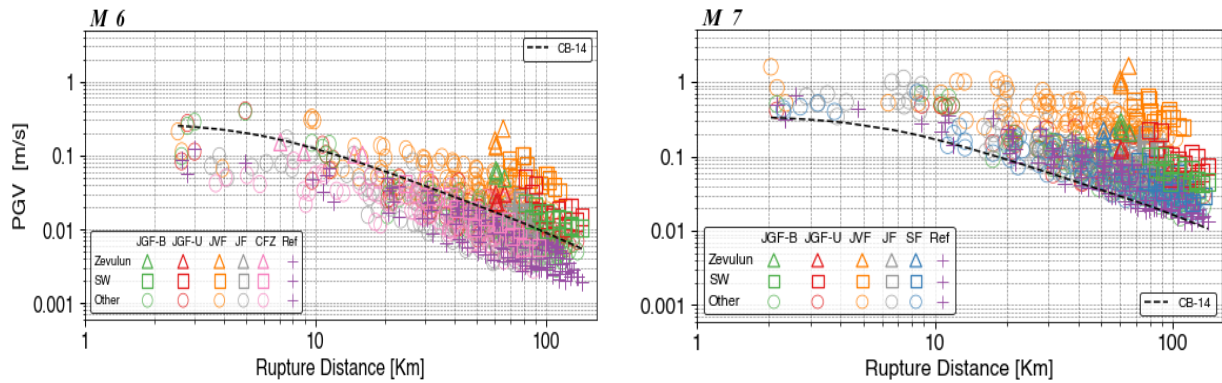
Fault Name	Scenario	Magnitude (M)	Rupture speed (m s^{-1})	Hypocentral depth (Km)
Jordan Gorge	Bilateral rupture (JGF-B)	6, 7	1800	11 and 13
Jordan Gorge	Southward unilateral rupture (JGF-U)	6, 7	1800	11 and 13
Jordan Valley	Bilateral super-shear rupture (JVF)	6, 7	1800	11 and 13
Jericho	Bilateral rupture (JF)	6, 7	3195	11 and 13
Shemona	Bilateral rupture (SF)	7	3195	13
Carmel	Bilateral rupture (CFZ)	6	3195	12
Reference	Bilateral rupture (Ref)	6, 7	3195	11 and 13

253 **4 Results**

254 In this section, we report the simulation results and the simulation-based attenuation model for M 6 and M 7. We
 255 begin with elaborating on the regression process and its deliverable, the attenuation model. Next, we show the
 256 correspondence of the model with the simulated database in terms of PGV residuals and examine the contribution
 257 of each earthquake scenario to the total deviation. Then, we proceed with looking into single station variability,
 258 through maps of the predicted and simulated PGV, with the corresponding residuals at each station. Finally, we
 259 examine the PGV and the 5 % - 95 % ground motions significant duration (D_s 595) correspondence between
 260 predicted by global GMM's (CB14, Afshari & Stewart, 2016, respectively) and simulated.

261 4.1 Simulation results

262 For each simulation, we attained a set of 129 synthetic ground motion records (3 components each; N-S, E-W,
 263 and vertical) from the network deployed in the computational domain. Next, we calculated the PGV values for
 264 each scenario at each station as the maximum value over the three components. We decided to exclude some of
 265 the M 7 near-source records (stations: 104,105 and 106 for the JVF scenario and stations: 122,123 and 129 for the
 266 JGF-B, JGF-U, and Shemona scenarios) due to high strain values and possible non-linear effects, not compatible
 267 with the linearity assumption of our model. In total, our ground motions database consists of 645 and 633 synthetic
 268 records for M 6 and M 7, respectively. Figure 5 presents our results in terms of PGV as a function of distance. We
 269 use different markers for records from the sedimentary structures of the Zevulun Valley and the Sedimentary
 270 wedge to differentiate them from the remaining data.



271 **Figure 4.** Simulation results, PGV-distance space, for bilateral rupture on the Jordan Gorge Fault (JGF-B), Jericho Fault (JF)
 272 Carmel Fault Zone (CFZ; for M 6) and the Shemona Fault (SF; for M 7), a southward unilateral rupture on the JGF (JGF-U),
 273 and a super-shear rupture on the Jordan Valley Fault (JVF); for M 6 (left) and M 7 (right). The records from Zevulun Valley
 274 and the Sedimentary wedge (SW) are marked with triangles and rectangles, respectively. The other records are marked with
 275 circles; the reference records are marked with pluses. For comparison, the CB14 is plotted for a strike-slip fault, $Z_{2.5}=0.42$
 276 Km and $V_{S30}=1686$ m/s (representing averaged values over all the sites).

277 4.2 Statistical analysis of ground motions results

278 The next step was to formulate a parametric ground motion attenuation model (AM) for the two magnitudes based
 279 on our simulations. Such a model will provide an estimate for the median ground motions and their variability.
 280 The general parametric form of the AM for both M 6 and M 7 is based on the CB14 function and presented in Eq.
 281 (1):

$$282 \ln Y = a \ln\left(\sqrt{R_{RUP}^2 + b}\right) + c \ln\left(\frac{V_{s,surf}}{V_{s,ref}}\right) + d Z_2 + e \pm \sigma \quad (1)$$

283 Where Y is ground motion intensity measure (IM). Due to the bandwidth of our numerical models (0.1 to 1 Hz),
 284 we formulated the AM in terms of PGV. We use the closest distance to the fault rupture plane (R_{RUP} as defined
 285 in CB14) as the initial explanatory variable. To improve the accuracy of the model, we incorporated two additional
 286 variables into the regressions: surface shear wave velocity at the site ($V_{s,surf}$) and the depth to $V_S = 2$ km s^{-1} (Z_2),
 287 which is the depth to the hard Mesozoic sediments (top Judea Gr.) considered the primary reflector in the region.
 288 a , b , c , d , and e are model coefficients, and σ is the standard deviation. The $V_{s,ref}$ is the shear wave velocity
 289 corresponding to the Judea Gr. in the computational domain, which in our model equals 2000 m s^{-1} .

290 The process of minimizing the residuals as a function of each explanatory variable can be found in the
 291 supplementary material (Fig. S3). We used $V_{S, \text{surf}}$ instead of the more common V_{S30} , as our grid resolution is 76
 292 m, preventing us from accurately determining the time-averaged shear wave velocity in the top 30 m of each site
 293 in our model. The coefficients and the total standard deviation for each model are summarized in Table 4.

294 **Table 4.** Regression coefficients for the attenuation model (AM)

Mag.	IM	a	b	c	d		e		Standard Deviation (σ)
					$R_{\text{rup}} > 58 \text{ km}$ and $z_2 > 0$	$R_{\text{rup}} < 58 \text{ km}$ or $z_2 = 0$	$R_{\text{rup}} > 58 \text{ km}$ and $z_2 > 0$	$R_{\text{rup}} < 58 \text{ km}$ or $z_2 = 0$	
6	PGV	-1.01	59.34	-0.685	0		0.56		0.6
7	PGV	-1.22	151.81	-0.669	0.56	0	2.08	2.42	0.629

295 4.3 AM Variability

296 We then examined the simulated data and the contribution of each scenario to the AM variability. We calculated
 297 the within-event (δW) and between-event (δB) residuals (see Al Atik et al., (2010)) for each magnitude and
 298 distance:

$$299 \delta W_{i,j} = \ln \text{PGV}_{i,j}^{\text{sim}} - \ln \text{PGV}_i^{\text{m}} \quad (2)$$

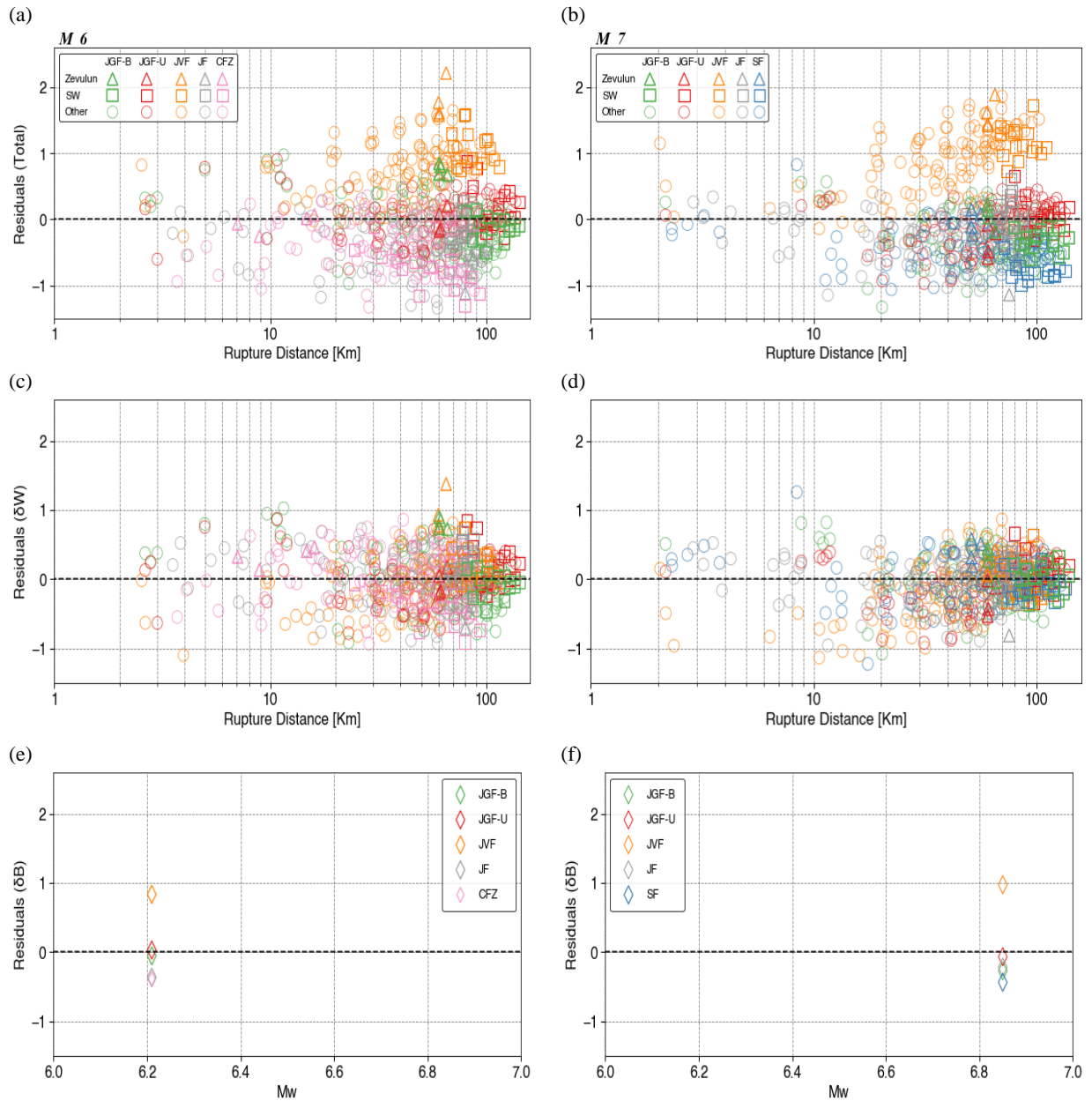
$$300 \delta B_i = \ln \text{PGV}_i^{\text{m}} - \ln \text{PGV}^{\text{AM}} \quad (3)$$

301 where $\text{PGV}_{i,j}^{\text{sim}}$ is the simulation value for event i and recording j , PGV_i^{m} is the median for event i , and PGV^{AM} is
 302 the AM median value. The total residual is the sum of the within and between event residuals.

303 The residuals are presented in Fig. 6: total (Fig. 6a and 6b), within-event (Fig. 6c and 6d), and between-
 304 events (Fig. 6e and 6f). The total residuals (Fig. 6a and 6b) show a large underprediction of the PGV from the
 305 JVF scenario (orange) on which we modeled a super-shear rupture, up to a ratio of 2.5 and 2 in the Zevulun Valley
 306 (orange triangles), for M 6 and M 7, respectively. However, the AM also exhibits over predictions; The PGV from
 307 the scenarios nucleated in the crystalline basement (SF, JF, and CFZ), with rupture speed= 3195 m s^{-1} , are
 308 overpredicted down to a ratio of more than -1 (in ln units).

309 Some within-event residuals exhibit distance dependency; for M 7, the JVF (super-shear model) and JGF-
 310 U (directivity model) residuals increase with rupture distances greater than 20 km. The JVF residuals also
 311 demonstrate the same distance dependency for M 6; however, the effect is less prominent when compared to M7.

312 The effect of the rupture directivity (JGF-U) is demonstrated in comparing the Zevulun Valley and the
 313 Sedimentary wedge within-event residuals (Fig. 6c and 6d). While in a symmetric rupture (JGF-B), the seismic
 314 energy dissipates equally into the north and south parts of the model, in an asymmetric rupture (JGF-U), more
 315 energy propagates toward the south, resulting in stronger ground motions at the Sedimentary wedge (Fig. 5).
 316 However, the ground motions are less intensive at the Zevulun Valley compared to the symmetric rupture. As a
 317 result, the within-event residuals for Zevulun Valley are higher for the JGF-B scenario compared to the JGF-U
 318 scenario, while for the Sedimentary wedge, the opposite is true. Most clearly, the JVF between-event residuals
 319 are the highest for both M 6 and M 7 with a ratio of 1 (Fig. 6e, and 6f).



320 **Figure 5.** Residuals between simulated and attenuation model (AM) PGV as a function of rupture distance (R_{RUP}), for bilateral
 321 rupture on the Jordan Gorge Fault (JGF-B), Jericho Fault (JF) Carmel Fault Zone (CFZ; for M 6) and the Shemona Fault (SF;
 322 for M 7), a southward unilateral rupture on the JGF (JGF-U), and a super-shear rupture on the Jordan Valley Fault (JVF); for
 323 M 6 (left) and M 7 (right); (a) and (b) total residuals, (c) and (d) within-event (δW) residuals, (e) and (f) between-event (δB)
 324 residuals. The records from Zevulun Valley and the Sedimentary wedge (SW) are marked with triangles and rectangles,
 325 respectively. The other records are marked with circles. Residuals are in ln units.

326 We further study the single station variation of ground motions and quantify the misfit between the
 327 simulated PGV and the AM PGV. We calculate the mean ground motion and its standard deviation at each station.
 328 The residuals for single station k were calculated as follows:

329
$$\delta_k = \ln PGV_k^{sim} - \ln PGV_k^{AM} \quad (4)$$

330 where PGV_k^{sim} and PGV_k^{AM} are the simulated and predicted mean PGV at station k, respectively. Figure 7 and
331 Figure 8 show the mean simulated and mean AM PGVs for M 6 and M 7, respectively. For each station, we also
332 plot the standard deviation using a scaled diameter circle.

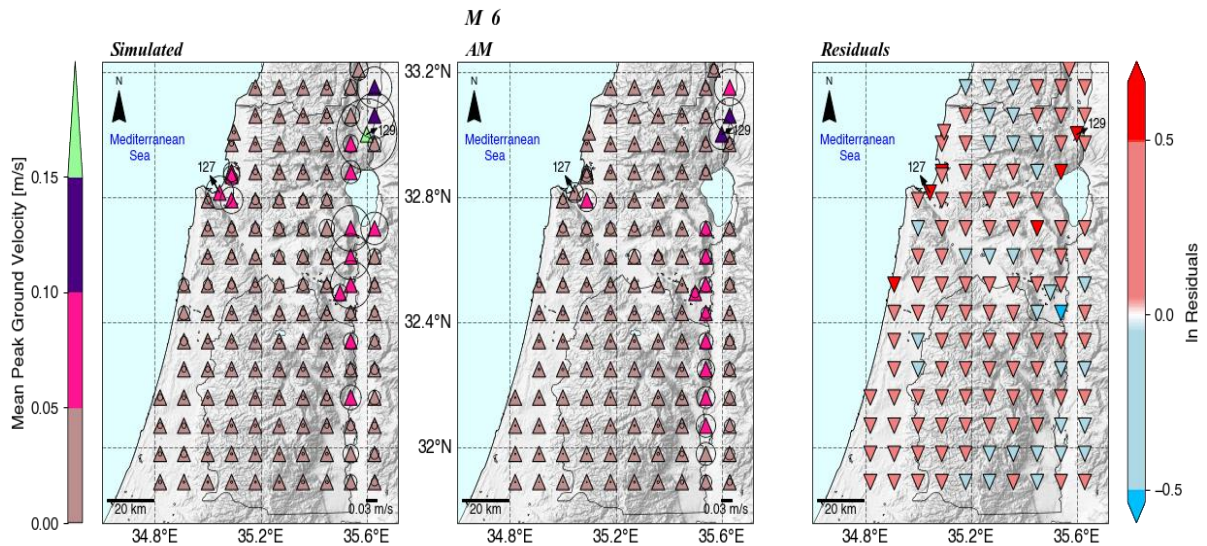
333 Both figures show that simulated ground motions variability at a single station is large, not fully covered
334 by the AM. For example, simulated ground motions at station 129 located on the Hula Valley exhibit a significant
335 standard deviation. For M 6, it is the largest value (green triangle) of 0.17 m s^{-1} compared to 0.09 m s^{-1} (indigo)
336 predicted by the AM, while for M 7, the largest standard deviation is 0.59 m s^{-1} (orange triangle) compared to
337 0.02 m s^{-1} (light green triangle) observed at station 127 located on the Zevulun Valley. As a result, there is a large
338 discrepancy between the simulated and AM values at specific stations.

339 In general, as expected from normal log distribution, higher mean PGV values are accompanied by a
340 larger standard deviation for both magnitudes. It is of significance for seismic hazard assessment, as outlier
341 ground motions at specific sites, mainly from $M < 7$ earthquakes, could be a significant source of damage
342 (Minson et al., 2020)

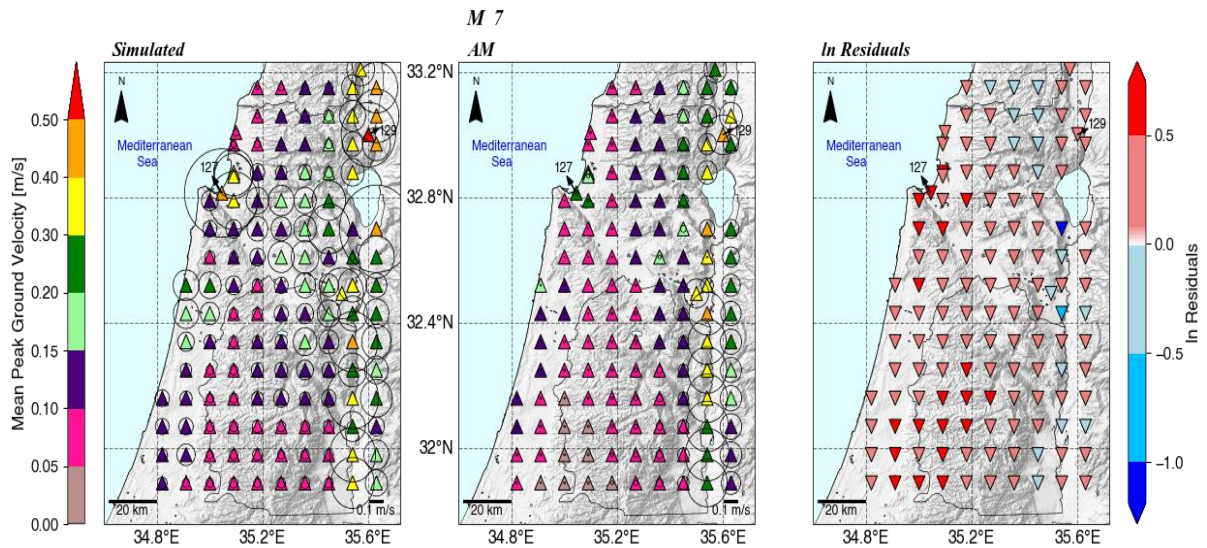
343 4.4 Comparison with global models

344 To examine the agreement between our simulations with an instrumental, global GMM, we calculated the total
345 residuals between PGVs from our simulations and PGVs predicted by the CB14 model. We chose the CB14 model
346 as it is planned to supersede the CB08 model used in the Israel Building Code (413). The CB14 PGVs were
347 calculated for a strike-slip fault, where we used the surface shear wave velocity as the V_{s30} parameter and the basin
348 response term Z_2 as $Z_{2.5}$. Figure 9 shows the total residuals for the AM and CB14 models as a function of distance
349 (R_{RUP}). For both magnitudes, the AM (mean and standard deviation) oscillates near the zero-model bias (black
350 horizontal dotted line). However, it deviates when approaching the region containing rupture distances typical of
351 the Zevulun Valley. The effect is more noticeable for M 7. Figure 9 also shows that the CB14 is less consistent
352 and performs differently for each magnitude. While for M 6, the GMM mostly over predicts (negative values) the
353 simulated PGV (until reaching ZV and SW rupture distances zones), for M 7, it mostly under predicts them
354 (positive values), except for large distances, up to a factor of 2 and above. In addition, the residuals calculated
355 with respect to CB14 exhibit a significant standard deviation of the mean ground motion, with considerably larger
356 variability for M 7.

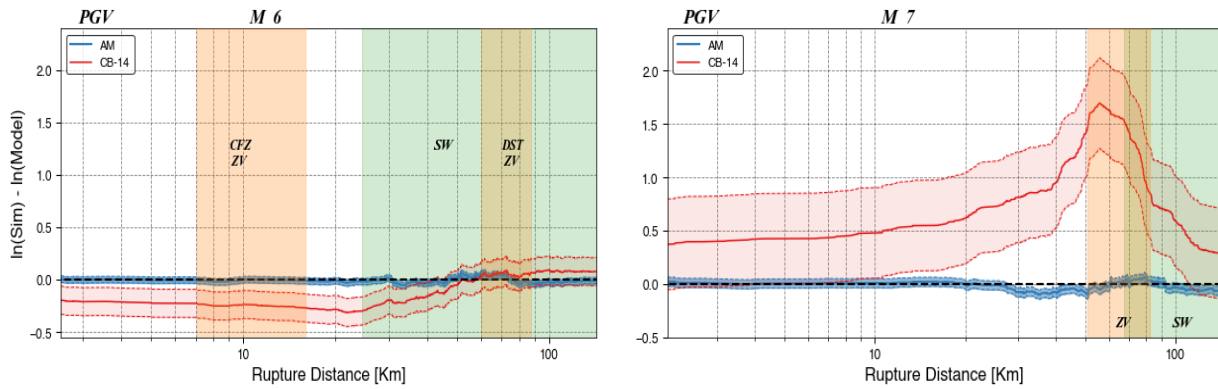
357 It is important to note that, by averaging the PGVs, we subdue the performance of both models at individual
358 stations/Rupture distances; thus, we cannot analyze the residual's spatial variations at a specific location.
359 However, it is sufficient to demonstrate that the global model deviates considerably from simulated ground
360 motions.



361 **Figure 6.** Map view of simulated and AM mean PGV (triangles) for M 6 and their standard deviation (diameters of the circles)
 362 at each station, with the respective residuals in ln units (inverted triangles).



363 **Figure 7.** Map view of simulated and AM mean PGV (triangles) for M 7 and their standard deviation (diameters of the circles)
 364 at each station, with the respective residuals in ln units (inverted triangles).

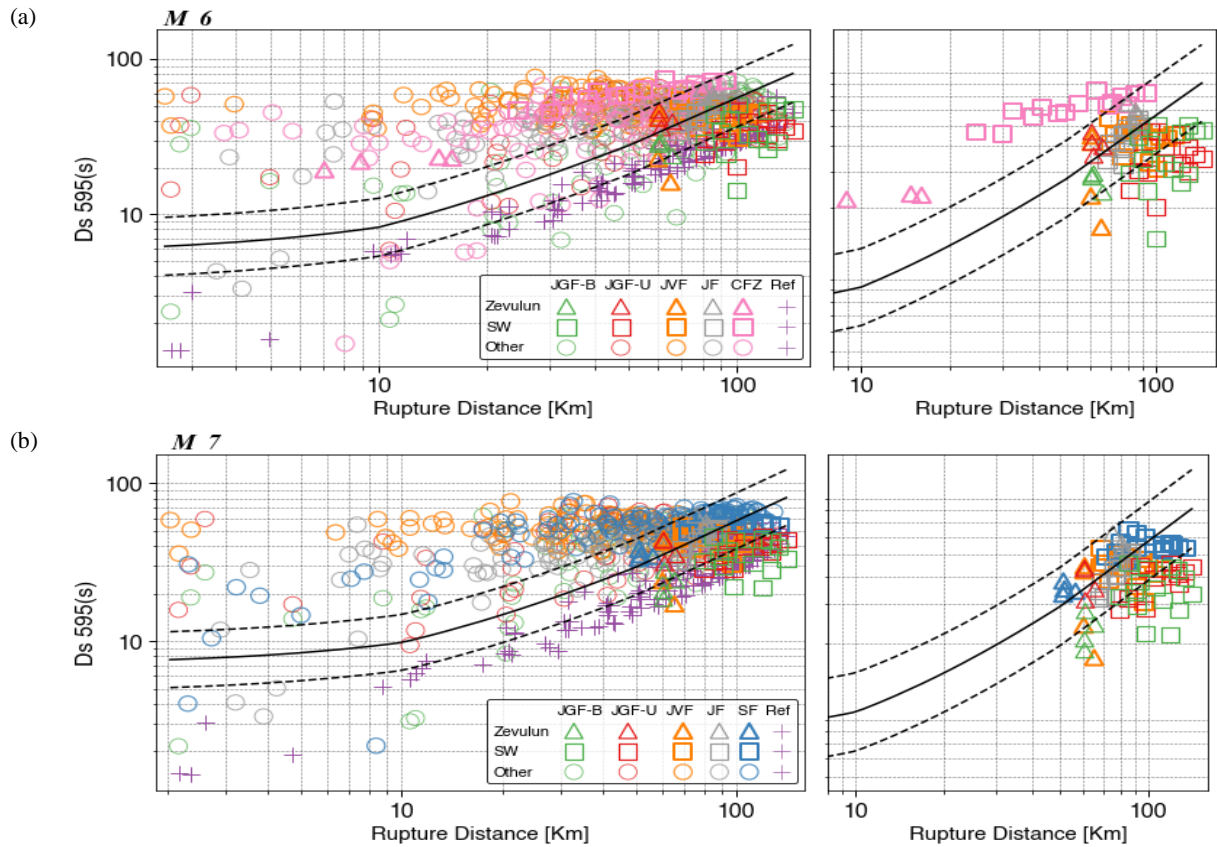


365 **Figure 8.** PGV Residuals between simulated (Sim) and predicted by the AM (blue) and CB14 (red) models, as a function of
 366 rupture distance (R_{RUP}), for M 6 (left) and M 7 (right). Thick lines represent the mean, and the shaded region denotes the
 367 standard deviation at each distance. The green and yellow shaded regions indicate the range of rupture distances related to the
 368 Sedimentary wedge (SW) and the Zevulun Valley (ZV), respectively. Residuals are in ln units.

369 4.5 Significant duration

370 Another important intensity measure is the significant duration (Ds_{595}), the time interval between 5 % to 95 %
 371 of the cumulative seismic energy (Arias Intensity) at a site. Figure 10 shows the simulated and empirical Ds_{595}
 372 values as a function of rupture distance. The typical increase of the empirical model with distance is captured in
 373 the reference (laterally homogenous) model. However, for all other models, the significant duration remains nearly
 374 constant, at ruptures distances larger than 20 km. In addition, the empirical GMM mostly under-predicts the
 375 simulated values between 2 to 50 Km for both magnitudes.

376 We postulate that this is caused by the complex geological setting of our model. The impact of geological
 377 complexity is reflected in Ds_{595} values from near-source stations, Zevulun Valley (triangles), and the
 378 Sedimentary wedge (rectangles). At near-source stations, the significant duration is large due to the effects of deep
 379 sedimentary structures along the DST, which also prolongs the path duration of the ground motions in other sites
 380 (Shimony et al., 2021), resulting in long significant duration with almost no path dependency. On the contrary at
 381 the Zevulun Valley and the SW, the energy accumulates faster than in other sites, as the ground motions are
 382 amplified, reaching 95 % of the total energy over a shorter duration. Interestingly, the significant duration in
 383 Zevulun Valley is lower than in the Sedimentary wedge. As we expect from deep sedimentary structures to
 384 prolong shaking duration, it may sound counterintuitive. However, it is explained by the relative proximity of the
 385 Zevulun Valley to the rupture. Whereas in Zevulun Valley, most of the energy arrives as a pulse at the beginning
 386 of the record, the energy at the more distant Sedimentary wedge accumulates more gradually and reaches its
 387 maximum almost at the end of the record, resulting in longer Ds_{595} values. In general, there is no large deviation
 388 between the simulated significant duration for M 6 and M 7. However, the empirical model shows a longer
 389 duration for M 7. This resembles in source duration is related to the DSM settings, more specifically to the source
 390 fundamental frequency, which in our study, is the same for both magnitudes; and it is a subject for testing in future
 391 works.



392 **Figure 9.** 5 % to 95 % ground motions significant duration ($D_s 595$) comparison between simulated and empirical GMM
 393 (Afshari and Stewart, 2016), for bilateral rupture on the Jordan Gorge Fault (JGF-B), Jericho Fault (JF) Carmel Fault Zone
 394 (CFZ; for M 6) and the Shemona Fault (SF; for M 7), a southward unilateral rupture on the JGF (JGF-U), and a super-shear
 395 rupture on the Jordan Valley Fault (JVF); for M 6 (a) and M 7 (b). Main plots (left) accompanied with subplots showing only
 396 the records from the Zevulun Valley and the Sedimentary wedge (right). Solid and dashed lines represent the median and the
 397 standard deviation of the empirical GMM, respectively. The records from Zevulun Valley and the Sedimentary wedge (SW)
 398 are marked with triangles and rectangles, respectively. The other records are marked with circles.

399 5 Discussion and Summary

400 A strong earthquake in Israel is imminent. However, up to date, a comprehensive regional GMM describing the
 401 spatial variability of ground motions has not yet been developed. This is mainly due to low seismicity rates and
 402 magnitude bounded strong motion database, coupled with sparse instrumental coverage. The current ground
 403 motion database lacks events with magnitude $M > 6$. To fill this gap and examine different source and path effects
 404 on ground motions variability, we simulated M 6 and M 7 earthquakes with different source and path properties.
 405 Subsequently, to study the ground motions variability, we developed a parametric attenuation model (AM) of
 406 PGV for M 6 and M 7 earthquakes, based on R_{RUP} , Z_2 , and $V_{s, surf}$ explanatory values.

407 Our analysis shows that the AM was unable to fully capture the variability of the simulated ground motions.
 408 Except for the Jordan Valley Fault (JVF) scenarios, the AM overestimates most of the modeled ground motions.
 409 We postulate that this overestimation results from the outlier, higher PGV values from the JVF scenario (Fig. 5),
 410 shifting the average ground motion toward them. Also, the within-event residuals for the JVF scenario show a
 411 distance dependency for $R_{RUP} > 20$ Km, continuing to grow away from the fault. We describe this scenario as a

412 "black swan" of our simulations and account its outlier behavior to the effects of the super-shear rupture, specific
413 to this model, affecting both the source and path terms of the ground motions (Fig.6). Super-shear ruptures behave
414 differently from sub-shear ruptures in many aspects. Most pertinent to our analysis is the slow energy decay of
415 the super-shears relative to sub-shears (Bhat et al., 2007); thus, it cannot be fully captured by our AM, which is
416 based mainly on sub-shear ruptures. In addition, it was found that Z_2 , depth to Mesozoic rock, has a very small
417 impact (<0.001) on the standard deviation for the M 6, reducing it from 0.5998 to 0.5988 (Fig. S3). As a result,
418 the M 6 model depends only on rupture distance and $V_{s, surf}$. For M 7, Z_2 is a good predictor for soil sites ($Z_2 > 0$)
419 located >58 Km from the source, including the Zevulun Valley and the Sedimentary wedge (Fig. 6d), imposing a
420 great seismic hazard. We do not see a clear dependence of the deep sedimentary structures with Z_2 , along the DST.
421 We speculate that Their site response may be masked by nearby source effects and requires additional analysis.

422 For each scenario, both magnitudes considered, we observed high PGV values at the Zevulun Valley and
423 the Sedimentary wedge associated with local site effects. These sedimentary structures exhibit a larger
424 discrepancy between the simulated and AM PGV values when compared with other sites. Such deviation indicates
425 that the AM does not fully capture the site effects of these complex structures, and future model refinements are
426 required. Likewise, the single station variability shows that the simulated values' highest mean and standard
427 deviation were in Zevulun Valley and near-source stations. In addition, a relatively high standard deviation was
428 also found in the Sedimentary wedge for M 7. This large single station variability is, apparently, the impact of the
429 outlier JVF PGV values. The AM does not account for the standard deviation at near-source and Zevulun Valley
430 stations for the M 6 and almost at all stations for the M 7. In fact, as the AM was unable to capture the simulated
431 JVF PGV values, it is expected that the single station variability cannot be captured either. Furthermore, we show
432 that the larger discrepancy for M 7 is due to the larger deviation of the JVFs ground motions from the mean (Fig.
433 6d,e).

434 Noteworthy to mention is that while the effect of the super-shear rupture on the AM performance is
435 systematic over the entire computational domain, the effect of the southward directivity is distance-dependent,
436 path effect, increasing towards the south, related to a larger amount of energy discharged in this direction.
437 Additional records of super-shear and directivity ruptures and accounting for these source effects by additional
438 model terms will improve the performance of the AM and will assist in better understanding the implications of
439 these phenomena on the seismic hazard in Israel.

440 The comparison of the simulated ground motions with a global GMM (CB14) showed that this model is
441 not well constrained for the simulated ground motions and does not capture their total variability. We note that
442 the comparison was performed on a single IM, the PGV values, one of several intensity measures provided by the
443 CB14. Thus, our findings are pertinent to the variability of PGV solely. It should be noted that PGV is a good
444 proxy for structural damage (e.g., to Kaestli & Fäh, (2006); Wald et al., (1999)), hence a crucial parameter for
445 seismic hazard mitigation. This discrepancy between modeled PGV and CB14 PGVs will inevitably result in a
446 discrepancy in the evaluation of structural damage.

447 The significant duration (DS595) comparison showed again that the imported model performs differently
448 than the simulated ground motion and cannot explain the local variability due to complex geological structure,
449 affecting the source, path, and site terms of the ground motions, such as the path independence of the significant
450 duration. However, we note that the Ds595 from our simulations were calculated based on low frequency content
451 (<1 Hz) and may be biased from Ds595 calculated based on the complete spectrum comprised of both low and

452 high frequencies. The effects of the frequency content on significant duration may be a potential topic for research
453 in future works.

454 Regional simulations of near-fault ground motions from large Mw 7 earthquakes in Lebanon, based on a
455 1-D velocity approximation, were presented by Fayjaloun et al., (2021). A comparison between the results
456 reported by Fayjaloun et al., (2021) with our results is somewhat limited. Specifically, it was shown that structural
457 and material heterogeneity of the crust in Israel results in regional ground motions variability (Volk et al., 2017;
458 Shani-Kadmiel et al., 2020; Shimony et al., 2021). These effects could only be captured by 3-D modelling.

459 We acknowledge that our AM is not independent of the evaluated models, thus describing both their
460 explanatory and predictive power (Mak et al., 2017). However, our goal was not to develop an independent and
461 comprehensive GMM but to study the ground motion variability through a parametric model. Recently, Maiti et
462 al., (2021) developed a suite of nine GMMs for Israel, in the magnitude range of 3 to 8 and distance range of 1 to
463 300 Km. These models are formulated in Fourier amplitude spectra (FAS) and are based on one empirical and
464 four simulated ground motion datasets and two empirical host models. The simulated ground motions were
465 generated using the Stochastic Method SIMulation (SMSIM) model of Boore (2003), with a unique set of
466 parameters for each simulation, calibrated with the empirical ground motions dataset (discussed in detail in
467 Yagoda-Biran et al., (2021)). However, the GMMs do not fully account for a local source, path, and site effects
468 due to sparse empirical database at large magnitudes ($M > 6$) and the utilization of a point-source stochastic
469 simulation method. This method is useful for simulating mean ground motions. Yet, it is less appropriate for
470 simulating site-specific and earthquake-specific ground motions and low-frequency ground motions, which are
471 affected by the 3D geometry of the computational domain. The AM presented in this work is based on 3D
472 simulations and incorporates a finite fault source with different rupture properties. This is the first step toward
473 developing a regional GMM, accounting for local source, path, and site effects. In subsequent work, which is
474 beyond the scope of the current research, we intend to develop a complete GMM for Israel, which will include all
475 the magnitudes and will be based on empirical ($M < 6$) as well as on synthetic ($M > 6$) databases. In addition, we
476 plan to incorporate new path and site terms such as $Z_{0.8}$ for the Zevulun valley and the Sedimentary wedge,
477 distance-dependent and rupture velocity-dependent attenuation for Directivity and super-shear ruptures, among
478 others; as well as a source term for super-shear ruptures. Such a model is expected to perform better than imported
479 global models by maintaining both; a lower aleatory variability and, as new synthetic data will be added to the
480 database, reduced epistemic uncertainty of the median ground motions (Abrahamson et al., 2019).

481 The population of Israel is fast-growing, with an annual rate of 1.8 % (OECD 2020 data), compared with
482 the 0.4 % average of the OECD. Coupled with fast economic growth of 4.5 % (OECD 2019 data), the demand for
483 housing and infrastructure constantly elevates the seismic risk in Israel. Our work shows that the ground motions
484 in Israel from M 6 and M 7 earthquakes are expected to be very damaging, up to 8-9 EMS (Fig. S4). Furthermore,
485 the modeled ground motions exhibit considerable spatial variability, which imported GMMs do not fully capture.
486 The development of a local comprehensive GMM model is therefore critical for the mitigation of seismic risk. In
487 the foreseen future, the moderate-strong ground motion data gap will be filled by synthetic ground motion records
488 from systematic numerical simulations.

489 **Data and resources**

490 Israel Seismic catalog (Fig. 1a), expanded after Wetzler & Kurzon (2016) catalog and the configuration of the
491 Israel seismic network (Fig. 1b) after Kurzon et al., (2020) can be found at
492 <https://earthquake.co.il/en/earthquake/searchEQS.php> and <https://earthquake.co.il/en/network/accNetwork.php>,
493 respectively. The ground motions database of Israel (Fig. 2) discussed in Yagoda-Biran et al., (2021) is available
494 at <https://earthquake.co.il/en/hazards/EngSeismology.php>. The Taub Center population projections for Israel are
495 accessible at <https://www.taubcenter.org.il/en/pr/population-projections-for-israel-2017-2040/>. OECD population
496 and economic growth rates can be found at <https://data.oecd.org/israel.htm#profile-economy>. Simulations were
497 performed using SW4 version 2.0 (v2.0; Petersson and Sjögreen, 2017a), an open-source package for wave
498 propagation simulations, available at github.com/geodynamics/sw4 (last accessed June 2021). Data processing
499 was done with the pySW4 package from Shahr Shani-Kadmiel, available at
500 <https://github.com/shaharkadmiel/pySW4> (last accessed July 2021), and "obspsy" (Beyreuther et al., 2010),
501 developed for numerical seismology. Figures were prepared with Matplotlib (Hunter, 2007) and Cartopy (Met
502 Office, 2016). Peak ground velocity (PGV) values, according to Campbell and Bozorgnia (2014), were calculated
503 using the Next Generation Attenuation-West Project (NGA-West2) ground-motion prediction equations (GMPEs)
504 excel file, available at <https://apps.peer.berkeley.edu/ngawest2/databases/> (last accessed July 2021). The
505 supplemental material includes: (1) synthetic station network deployed in our models (Fig. S1); (2) distributed
506 slip model (DSM) slip distribution and rupture time (Fig. S2); (3) the evolution of the residuals between simulated
507 and attenuation model (AM) PGV for M 6 and M 7 (Fig. S3) and (4) map view of simulated mean EMS intensity
508 calculated according to Kaestli & Fäh, (2006).

509 *Competing interests.* The authors declare that they have no conflict of interest.

510 **Acknowledgments**

511 This research was partially funded by the Ministry of Energy, Israel (Grant Number 219-17-02). Co-author JG
512 was partially supported by the Ministry of Energy scholarship for graduate studies (Tender 76/19).

513 **References**

- 514 Abrahamson, N. A., Kuehn, N. M., Walling, M., and Landwehr, N.: Probabilistic seismic hazard analysis in
515 california using nonergodic ground-motion models, *Bull. Seismol. Soc. Am.*, 109, 1235–1249,
516 <https://doi.org/10.1785/0120190030>, 2019.
- 517 Afshari, K. and Stewart, J. P.: Physically parameterized prediction equations for significant duration in active
518 crustal regions, *Earthq. Spectra*, 32, 2057–2081, <https://doi.org/10.1193/063015EQS106M>, 2016.
- 519 Agnon, A.: Pre-instrumental earthquakes along the Dead Sea rift, in: *Modern Approaches in Solid Earth*
520 *Sciences*, vol. 6, Springer, 207–261, https://doi.org/10.1007/978-94-017-8872-4_8, 2014.
- 521 Aldersons, F., Ben-Avraham, Z., Hofstetter, A., Kissling, E., and Al-Yazjeen, T.: Lower-crustal strength under
522 the Dead Sea basin from local earthquake data and rheological modeling, *Earth Planet. Sci. Lett.*, 214, 129–142,
523 [https://doi.org/10.1016/S0012-821X\(03\)00381-9](https://doi.org/10.1016/S0012-821X(03)00381-9), 2003.
- 524 Ambraseys, N. N.: Comparison of frequency of occurrence of earthquakes with slip rates from long-term

525 seismicity data: The cases of Gulf of Corinth, Sea of Marmara and Dead Sea Fault Zone, *Geophys. J. Int.*, 165,
526 516–526, <https://doi.org/10.1111/j.1365-246X.2006.02858.x>, 2006.

527 Anderson, J. G. and Brune, J. N.: Probabilistic seismic hazard analysis without the ergodic assumption, *Seismol.*
528 *Res. Lett.*, 70, 19–28, <https://doi.org/10.1785/gssrl.70.1.19>, 1999.

529 Al Atik, L., Abrahamson, N., Bommer, J. J., Scherbaum, F., Cotton, F., and Kuehn, N.: The variability of
530 ground-motion prediction models and its components, *Seismol. Res. Lett.*, 81, 794–801,
531 <https://doi.org/10.1785/gssrl.81.5.794>, 2010.

532 Bartov, Y., Steinitz, G., Eyal, M., and Eyal, Y.: Sinistral movement along the Gulf of Aqaba - Its age and
533 relation to the opening of the Red Sea, *Nature*, 285, 220–222, <https://doi.org/10.1038/285220a0>, 1980.

534 Ben-Avraham, Z., Ginzburg, A., Makris, J., and Eppelbaum, L.: Crustal structure of the Levant Basin, eastern
535 Mediterranean, 346, 23–43, [https://doi.org/10.1016/S0040-1951\(01\)00226-8](https://doi.org/10.1016/S0040-1951(01)00226-8), 2002.

536 Beyreuther, M., Barsch, R., Krischer, L., Megies, T., Behr, Y., and Wassermann, J.: ObsPy: A python toolbox
537 for seismology, *Seismol. Res. Lett.*, 81, 530–533, <https://doi.org/10.1785/gssrl.81.3.530>, 2010.

538 Bhat, H. S., Dmowska, R., King, G. C. P., Klinger, Y., and Rice, J. R.: Off-fault damage patterns due to
539 supershear ruptures with application to the 2001 Mw 8.1 Kokoxili (Kunlun) Tibet earthquake, *J. Geophys. Res.*
540 *Solid Earth*, 112, 1–19, <https://doi.org/10.1029/2006JB004425>, 2007.

541 Boore, D. M.: Simulation of ground motion using the stochastic method, *Pure Appl. Geophys.*, 160, 635–676,
542 <https://doi.org/10.1007/PL00012553>, 2003.

543 Brocher, T. M.: Key elements of regional seismic velocity models for long period ground motion simulations, *J.*
544 *Seismol.*, 12, 217–221, <https://doi.org/10.1007/s10950-007-9061-3>, 2008.

545 Campbell, K. W. and Bozorgnia, Y.: NGA ground motion model for the geometric mean horizontal component
546 of PGA, PGV, PGD and 5% damped linear elastic response spectra for periods ranging from 0.01 to 10 s,
547 *Earthq. Spectra*, 24, 139–171, <https://doi.org/10.1193/1.2857546>, 2008.

548 Campbell, K. W. and Bozorgnia, Y.: NGA-West2 ground motion model for the average horizontal components
549 of PGA, PGV, and 5% damped linear acceleration response spectra, *Earthq. Spectra*, 30, 1087–1114,
550 <https://doi.org/10.1193/062913EQS175M>, 2014.

551 Chaljub, E., Moczo, P., Tsuno, S., Bard, P. Y., Kristek, J., Käser, M., Stupazzini, M., and Kristekova, M.:
552 Quantitative comparison of four numerical predictions of 3D ground motion in the Grenoble Valley, France,
553 *Bull. Seismol. Soc. Am.*, 100, 1427–1455, <https://doi.org/10.1785/0120090052>, 2010.

554 Douglas, J. and Aochi, H.: A survey of techniques for predicting earthquake ground motions for engineering
555 purposes, *Surv. Geophys.*, 29, 187–220, <https://doi.org/10.1007/s10712-008-9046-y>, 2008.

556 Fayjaloun, R., Dabaghi, M., Cornou, C., Causse, M., Lu, Y., Stehly, L., Voisin, C., and Mariscal, A.: Hybrid
557 Simulation of Near-Fault Ground Motion for a Potential Mw 7 Earthquake in Lebanon, *Bull. Seismol. Soc. Am.*,
558 111, 2441–2462, <https://doi.org/10.1785/0120210091>, 2021.

559 Garfunkel, Z.: Lateral motion and deformation along the Dead Sea transform, in: *Modern Approaches in Solid*
560 *Earth Sciences*, vol. 6, Springer International Publishing, 109–150, https://doi.org/10.1007/978-94-017-8872-4_5, 2014.

562 Graves, R. and Pitarka, A.: Refinements to the Graves and Pitarka (2010) broadband ground-motion simulation
563 method, *Seismol. Res. Lett.*, 86, 75–80, <https://doi.org/10.1785/0220140101>, 2015.

564 Graves, R., Jordan, T. H., Callaghan, S., Deelman, E., Field, E., Juve, G., Kesselman, C., Maechling, P., Mehta,

565 G., Milner, K., Okaya, D., Small, P., and Vahi, K.: CyberShake: A Physics-Based Seismic Hazard Model for
566 Southern California, *Pure Appl. Geophys.*, 168, 367–381, <https://doi.org/10.1007/s00024-010-0161-6>, 2011.

567 Grünthal, G., Hakimhashemi, A., Schelle, H., Bosse, C., and Wahlström, R.: The long-term temporal behaviour
568 of the seismicity of the Dead Sea Fault Zone and its implication for time-dependent seismic hazard assessments,
569 <https://doi.org/10.2312/GFZ.b103-09098>, 2009.

570 Gvirtzman, Z., Zilberman, E., and Folkman, Y.: Reactivation of the Levant passive margin during the late
571 Tertiary and formation of the Jaffa Basin offshore central Israel, *J. Geol. Soc. London.*, 165, 563–578,
572 <https://doi.org/10.1144/0016-76492006-200>, 2008.

573 Gvirtzman Z., I. M. and Sagee, Y.: Re-processing and geological re-interpretation of old seismic lines of Haifa
574 bay, *Geol. Surv. Isr. GSI/27/2011*, 2011.

575 Gvitzman, Z. and Zaslavsky, Y.: Map of Zones with Potentially High Ground Motion Amplification:
576 Explanatory Notes, Rep. Num. GSI/15/2009, 2009.

577 Hamiel, Y., Amit, R., Begin, Z. B., Marco, S., Katz, O., Salamon, A., Zilberman, E., and Porat, N.: The
578 seismicity along the dead sea fault during the last 60,000 years, *Bull. Seismol. Soc. Am.*, 99, 2020–2026,
579 <https://doi.org/10.1785/0120080218>, 2009.

580 Hamiel, Y., Piatibratova, O., and Mizrahi, Y.: Creep along the northern Jordan Valley section of the Dead Sea
581 Fault, *Geophys. Res. Lett.*, 43, 2494–2501, <https://doi.org/10.1002/2016GL067913>, 2016.

582 Hunter, J. D.: Matplotlib: A 2D graphics environment, *Comput. Sci. Eng.*, 9, 90–95,
583 <https://doi.org/10.1109/MCSE.2007.55>, 2007.

584 Israel Standards Institution: Standard SI 413. Design Provisions for Earthquake Resistance of Structures.
585 Amendment No. 5, 2013.

586 Kaestli, P. and Fäh, D.: Rapid estimation of macroseismic effects and Shakemaps using macroseismic data, in:
587 1st European Conf. Earthquake Engineering and Seismology, 1535, 2006.

588 Kuehn, N. M., Abrahamson, N. A., and Walling, M. A.: Incorporating nonergodic path effects into the NGA-
589 west2 ground-motion prediction equations, *Bull. Seismol. Soc. Am.*, 109, 575–585,
590 <https://doi.org/10.1785/0120180260>, 2019.

591 Kurzon, I., Nof, R. N., Laporte, M., Lutzky, H., Polozov, A., Zakosky, D., Shulman, H., Goldenberg, A.,
592 Tatham, B., and Hamiel, Y.: The “TRUAA” seismic network: Upgrading the Israel Seismic Network-toward
593 national earthquake early warning system, *Seismol. Res. Lett.*, 91, 3236–3255,
594 <https://doi.org/10.1785/0220200169>, 2020.

595 Lan, X., Xing, H., Zhou, J., and Zhao, J. X.: A comparison of the source, path, and site effects of the strong-
596 motion records from the western and the southwestern parts of China with modern ground-motion prediction
597 equations, *Bull. Seismol. Soc. Am.*, 109, 2691–2709, <https://doi.org/10.1785/0120180293>, 2019.

598 Maiti, S. K., Yagoda-Biran, G., and Kamai, R.: A Suite of Alternative Ground-Motion Models (GMMs) for
599 Israel, *Bull. Seismol. Soc. Am.*, 111, 2177–2194, <https://doi.org/10.1785/0120210003>, 2021.

600 Mak, S., Cotton, F., and Schorlemmer, D.: Measuring the performance of ground-motion models: The
601 importance of being independent, <https://doi.org/10.1785/0220170097>, 2017.

602 Met Office: Cartopy: a cartographic python library with a matplotlib interface, <http://scitools.org.uk/cartopy>,
603 2016.

604 Minson, S. E., Baltay, A. S., Cochran, E. S., McBride, S. K., and Milner, K. R.: Shaking is almost always a

605 surprise: The earthquakes that produce significant ground motion, *Seismol. Res. Lett.*, 92, 460–468,
606 <https://doi.org/10.1785/0220200165>, 2020.

607 Mizutori, M. and D’ebarati, G.: The human cost of disasters: an overview of the last 20 years (2000-2019), UN
608 Off. Disaster Risk Reduction., <https://doi.org/10.18356/79b92774-en>, 2020.

609 Pesaresi, M., Ehrlich, D., Kemper, T., Siragusa, A., Florczyk, A., Freire, S., and Corbane, C.: Atlas of the
610 Human Planet 2017. Global Exposure to Natural Hazards. EUR 28556 EN, 92 pp., 2017.

611 Petersson, N. A. and Sjogreen, B.: SW4 Users Guide, Lawrence Livermore Natl. Lab. Tech. Rep. LLNL-SM,
612 662014, 2014.

613 Petersson, N. A. and Sjogreen, B.: SW4, version 2.0, Computational Infrastructure of Geodynamics,
614 <https://doi.org/10.5281/zenodo.1045297>, 2017a.

615 Petersson, N. A. and Sjogreen, B.: User’s guide to SW4, version 2.0, LLNL-SM-741439., [https://doi.org/.](https://doi.org/),
616 2017b.

617 Pitarka, A., Akinci, A., De Gori, P., and Buttinelli, M.: Deterministic 3D Ground-Motion Simulations (0–5 Hz)
618 and Surface Topography Effects of the 30 October 2016 Mw 6.5 Norcia, Italy, *Earthquake, Bull. Seismol. Soc.*
619 *Am.*, <https://doi.org/10.1785/0120210133>, 2021.

620 Rosenthal, M., Ben-Avraham, Z., and Schattner, U.: Almost a sharp cut – A case study of the cross point
621 between a continental transform and a rift, based on 3D gravity modeling, 761, 46–64,
622 <https://doi.org/10.1016/j.tecto.2019.04.012>, 2019.

623 Rybakov, M., Fleischer, L., and ten Brink, U.: The Hula Valley subsurface structure inferred from gravity data,
624 *Isr. J. Earth Sci.*, 52, 113–122, <https://doi.org/10.1560/WF6V-4BVG-GXQM-PKVR>, 2003.

625 Sadeh, M., Hamiel, Y., Ziv, A., Bock, Y., Fang, P., and Wdowinski, S.: Crustal deformation along the Dead Sea
626 Transform and the Carmel Fault inferred from 12 years of GPS measurements, *J. Geophys. Res. Solid Earth*,
627 117, <https://doi.org/10.1029/2012JB009241>, 2012.

628 Shamir, G., Bartov, Y., Sneh, A., Fleisher, L., Arad, V., and Rosensaft, M.: Preliminary seismic zonation in
629 Israel, *earthquake.co.il*28 , pp., 2001.

630 Shani-Kadmie, S., Tsesarsky, M., and Gvirtzman, Z.: Distributed slip model for forward modeling strong
631 Earthquakes, *Bull. Seismol. Soc. Am.*, 106, 93–103, <https://doi.org/10.1785/0120150102>, 2016.

632 Shani-Kadmiel, S., Volk, O., Gvirtzman, Z., and Tsesarsky, M.: Ground motion amplification atop the complex
633 sedimentary basin of Haifa Bay (Israel), *Bull. Earthq. Eng.*, 18, 821–836, [https://doi.org/10.1007/s10518-018-](https://doi.org/10.1007/s10518-018-00533-9)
634 00533-9, 2020.

635 Shi, Z. and Ben-Zion, Y.: Dynamic rupture on a bimaterial interface governed by slip-weakening friction,
636 *Geophys. J. Int.*, 165, 469–484, <https://doi.org/10.1111/j.1365-246X.2006.02853.x>, 2006.

637 Shimony, R., Gvirtzman, Z., and Tsesarsky, M.: Seismic energy release from intra-basin sources along the dead
638 sea transform and its influence on regional ground motions, *Bull. Seismol. Soc. Am.*, 111, 295–308,
639 <https://doi.org/10.1785/0120200215>, 2021.

640 Volk, O., Shani-Kadmiel, S., Gvirtzman, Z., and Tsesarsky, M.: 3D effects of sedimentary wedges and
641 subsurface canyons: Ground-motion amplification in the Israeli coastal plain, *Bull. Seismol. Soc. Am.*, 107,
642 1324–1335, <https://doi.org/10.1785/0120160349>, 2017.

643 Wald, D. J., Quitoriano, V., Heaton, T. H., and Kanamori, H.: Relationships between peak ground acceleration,
644 peak ground velocity, and modified mercalli intensity in California, *Earthq. Spectra*, 15, 557–564,

645 <https://doi.org/10.1193/1.1586058>, 1999.

646 Walling, M. . and Abrahamson, N. .: Non-Ergodic Probabilistic Seismic Hazard Analyses, in: 15th World
647 Conference on Earthquake Engineering (15WCEE). Lisbon, Portugal, 24-28 September, 2012.

648 Wang, Z.: A Clear Definition of Seismic Hazard and Risk: A Basis for Hazard and Risk Assessment,
649 Communication, and Management, Am. Geophys. Union, 2005, S53B-1110, 2005.

650 Wells, D. L. and Coppersmith, K. J.: New empirical relationships among magnitude, rupture length, rupture
651 width, rupture area, and surface displacement, Bull. - Seismol. Soc. Am., 84, 974–1002, 1994.

652 Wetzler, N. and Kurzon, I.: The earthquake activity of Israel: Revisiting 30 years of local and regional seismic
653 records along the dead sea transform, Seismol. Res. Lett., 87, 47–58, <https://doi.org/10.1785/0220150157>, 2016.

654 Yagoda-Biran, G., Maiti, S. K., Wetzler, N., Nof, R. N., Pashcur, Y., and Kamai, R.: A ground-motion database
655 for Israel with its corresponding point-source parameters, for engineering seismology applications, Seismol.
656 Res. Lett., 92, 2679–2690, <https://doi.org/10.1785/0220200477>, 2021.

657 Zohar, M.: Temporal and spatial patterns of seismic activity associated with the Dead Sea transform (DST)
658 during the past 3000 yr, Seismol. Res. Lett., 91, 207–221, <https://doi.org/10.1785/0220190124>, 2019.

659